





# Lysosomal protein transmembrane 5 promotes lung-specific metastasis by regulating BMPR1A lysosomal degradation

Bo Jiang<sup>1,5</sup>, Xiaozhi Zhao<sup>1,5</sup>, Wei Chen<sup>1</sup>, Wenli Diao<sup>1</sup>, Meng Ding<sup>1</sup>, Haixiang Qin<sup>1</sup>, Binghua Li<sup>2</sup>, Wenmin Cao<sup>1</sup>, Wei Chen<sup>1</sup>, Yao Fu<sup>3</sup>, Kuiqiang He<sup>1</sup>, Jie Gao<sup>1</sup>, Mengxia Chen<sup>1</sup>, Tingsheng Lin<sup>1</sup>, Yongming Deng<sup>1</sup>, Chao Yan<sup>4</sup>   & Hongqian Guo<sup>1</sup>  

Organotropism during cancer metastasis occurs frequently but the underlying mechanism remains poorly understood. Here, we show that lysosomal protein transmembrane 5 (LAPTM5) promotes lung-specific metastasis in renal cancer. LAPTM5 sustains self-renewal and cancer stem cell-like traits of renal cancer cells by blocking the function of lung-derived bone morphogenetic proteins (BMPs). Mechanistic investigations showed that LAPTM5 recruits WWP2, which binds to the BMP receptor BMPR1A and mediates its lysosomal sorting, ubiquitination and ultimate degradation. BMPR1A expression was restored by the lysosomal inhibitor chloroquine. LAPTM5 expression could also serve as an independent predictor of lung metastasis in renal cancer. Lastly, elevation of LAPTM5 expression in lung metastases is a common phenomenon in multiple cancer types. Our results reveal a molecular mechanism underlying lung-specific metastasis and identify LAPTM5 as a potential therapeutic target for cancers with lung metastasis.

<sup>1</sup>Department of Urology, Nanjing Drum Tower Hospital, the Affiliated Hospital of Nanjing University Medical School, Institute of Urology, Nanjing University, Nanjing, Jiangsu 210008, China. <sup>2</sup>Department of Hepatobiliary Surgery, Nanjing Drum Tower Hospital, the Affiliated Hospital of Nanjing University Medical School, Nanjing, Jiangsu 210008, China. <sup>3</sup>Department of Pathology, Nanjing Drum Tower Hospital, the Affiliated Hospital of Nanjing University Medical School, Nanjing, Jiangsu 210008, China. <sup>4</sup>State Key Laboratory of Pharmaceutical Biotechnology, School of Life Sciences, Nanjing University, Nanjing, China. <sup>5</sup>These authors contributed equally: Bo Jiang, Xiaozhi Zhao. ✉email: [yanchao@nju.edu.cn](mailto:yanchao@nju.edu.cn); [dr.ghq@nju.edu.cn](mailto:dr.ghq@nju.edu.cn)

**M**etastasis is involved in 90% of cancer-related mortality and blocking metastasis remains a major challenge for cancer treatment<sup>1</sup>. In clinical practice, it is frequently observed that primary tumors have the proclivity to often metastasize and colonize specific organs, for instance, breast cancer (BCa) often metastasizes to the brain, prostate cancer (PCa) to the bone and renal cancer (RCC) to the lung<sup>2,3</sup>. Tumors with different organ metastases often show distinct responses to treatments and prognoses<sup>4,5</sup>, the mechanism of which is not well understood, presenting an unanswered scientific question and a promising therapeutic opportunity for cancer treatment.

Metastatic dissemination occurs frequently in the early stage of tumor development but the clinical manifestation of metastases often takes years<sup>6–8</sup> because a vast majority of tumor cells that infiltrate the parenchyma of an organ are rejected by organ-specific inhibitory signals (e.g., bone morphogenetic proteins (BMPs) in the lung stroma; Wnt family member 5a (Wnt5a), transforming growth factor Beta 2 (TGF- $\beta$ 2) and growth differentiation factor 10 (GDF10) in the bone stroma), or aboriginal cells (like astrocytes in the brain parenchyma and osteoblasts in the bone stroma), and are eventually destroyed or enter a dormant state<sup>9–12</sup>. However, certain genetic mutations or molecular characteristics enable a small fraction of tumor cells, sometimes called metastasis-initiating cells, to interact with aboriginal cells and/or overcome these inhibitory signals, and maintain cancer stem cell-like traits and eventually colonize target organs<sup>13–17</sup>. It is now known that unique expression patterns of certain molecules in cancer cells mediate their selective interaction with target organs and drive organ-specific metastasis. For example, Coco, a BMP antagonist, mediates lung-specific metastasis, and Cx43-PCDH7 junction formation triggers brain metastasis in BCa<sup>15,18–21</sup>. However, the molecular basis underlying lung-specific metastasis in most cancers remains unclear. In RCC, for instance, metastases from different organs display unique genetic alterations. Loss of chromosome 8p and 18q, along with gain of chromosome 12, are found very frequently in lung metastases<sup>22,23</sup>. In particular, organ-specific metastases not only share the vast majority of mutations with, but also possess characteristic evolutionary offshoots of, their parental primary tumors and other organ metastases<sup>24–26</sup>. Moreover, patients with lung metastasis seem to show a better survival rate, whereas bone and liver metastasis are associated with worse tyrosine kinase inhibitor (TKI) response and poor prognosis<sup>27–29</sup>. The cause of this clinical manifestation is still unclear.

In this work, we explore the mechanism that drives the lung-specific metastasis of RCC. We find that lysosomal protein transmembrane 5 (LAPTM5) promotes lung-specific metastasis in RCC patients. Mechanistic studies suggest that LAPTM5 exerts this function by promoting lysosomal sorting and degradation of BMP receptor 1A (BMPRIA), thereby enhancing the self-renewal capability of metastasis-initiating cells in the lung microenvironment.

## Results

**Establishment of RCC cell lines with high lung metastasis tendency.** We first generated organ-specific metastatic derivatives of RCC by repeated intracardiac (I.C.) inoculation and metastases clone selection/expansion, using a luciferase-labeled murine RCC cell line Renca<sup>luci</sup> (Fig. 1a). In keeping with the clinical manifestations of RCC<sup>2</sup>, the Renca<sup>luci</sup> cells mainly metastasized to the lung, bone, and brain (Supplementary Fig. 1a, b and Fig. 1b). The resulting subpopulations were named by their source organ and generation, e.g., lung metastatic derivative-1a, Renca<sup>LuM1a</sup>, is a lung metastatic derivative after the first round of selection (Fig. 1c). Intriguingly, different organ derivatives showed distinct cell morphology but similar proliferation rates in vitro

(Supplementary Fig. 1c, d). The above experiments were also repeated with the human RCC cell line 786O<sup>luci/eGFP</sup> (dual-labeled with luciferase and eGFP) in the immunodeficient NOD/SCID mice but only the lung derivatives were selected (Supplementary Fig. 1e, f), similar results to that of the murine cell line were observed (Supplementary Fig. 1g, h).

To assess the lung metastasis-forming ability of the organ-specific derivatives, representative Renca<sup>luci</sup> parental and derivative cells were inoculated into the arterial circulation of BALB/c mice and analyzed for lung metastasis. The lung-met derivative Renca<sup>LuM2b</sup> metastasized to the lung in 75% (6/8) of the mice 11 days post injection, compared to 10% (1/10) in the parental line, 12.5% (1/8) in the brain-met Renca<sup>BrM2b</sup>, and 0% (0/9) in the bone-met Renca<sup>BoM2</sup> cell line (Fig. 1d). Mice inoculated with Renca<sup>LuM2b</sup> cells exhibited shorter survival than the parental Renca<sup>luci</sup> group (Fig. 1e). Increased lung metastasis activity was also confirmed by ex vivo imaging of excised lungs in mice inoculated with the Renca<sup>LuM2b</sup> or 786O<sup>LuM1a</sup> derivatives (Fig. 1f, g). These data demonstrated that we have successfully modeled the multi-organ metastasis of RCC and obtained RCC cell derivatives with high lung metastasis tendency.

## LAPTM5 mediates lung metastasis, but not brain or bone metastasis.

We next performed genome-wide transcriptional profiling to identify molecules associated with different metastatic phenotypes. Principal component analysis (PCA) revealed the adjacent clustering of the Renca<sup>LuM2b</sup> derivative with the Renca<sup>BrM2b</sup> derivative, away from the Renca<sup>luci</sup> cells and the Renca<sup>BoM2</sup> derivative (Supplementary Fig. 2a, b and Fig. 2a); this is consistent with a previous study, which suggested the presence of common mediators in pulmonary and cerebral metastases<sup>20</sup>. To identify the key molecules associated with lung-specific metastasis, we compared the Renca<sup>LuM2b</sup> derivative with Renca<sup>luci</sup>, Renca<sup>BoM2</sup> and Renca<sup>BrM2b</sup>, and identified 562, 942 and 276 genes, respectively, that were highly expressed in Renca<sup>LuM2b</sup> (Supplementary Fig. 2c–e). Of these upregulated genes, 69 were present in all sets (Fig. 2b and Supplementary Data 1). In addition, we analyzed an independent human RCC dataset (Jon\_Renal\_Cancer)<sup>30</sup> and found 760 probes/genes that displayed higher expression levels in lung metastases (L-Mets) compared with primary RCC (pri-RCC) (Supplementary Fig. 2f, g). Integrated analysis of these two datasets identified three genes: cathepsin S (*CTSS*), lysosomal protein transmembrane 5 (*LAPTM5*), and insulin-like growth factor binding protein 5 (*IGFBP5*), that appeared to be activated specifically in RCC cells from lung metastases in both datasets (Fig. 2b and Supplementary Data 2). Among these three genes, *LAPTM5* showed much more prominent elevation than *CTSS* and *IGFBP5* in lung derivatives (Fig. 2c). Moreover, *LAPTM5*, a lysosomal-associated multi-spanning membrane protein<sup>31</sup>, not only exhibited higher transcription levels in the Renca<sup>LuM2b</sup> lung derivative, but also in clinical specimens from the L-Mets and primary RCC with lung metastasis (RCCL) subgroups, compared with the pri-RCC subgroup (Supplementary Data 2). Importantly, elevated transcription and translation of the *LAPTM5* gene was only observed in the lung metastasis derivatives but not in brain or bone metastasis (Fig. 2c, d). These data suggested that *LAPTM5* might be associated with lung metastasis of RCC. These results were also validated by immunohistochemical (IHC) analysis of different tissues in the mouse model (Fig. 2e). To strengthen these findings, we directly injected Renca<sup>luci</sup> cells through mice tail vein and isolated three generations of cell derivatives from lung metastases; higher *LAPTM5* levels were detected in two of three metastatic clones, further confirming the differential expression of *LAPTM5* in lung metastases (Supplementary Fig. 3a, b).

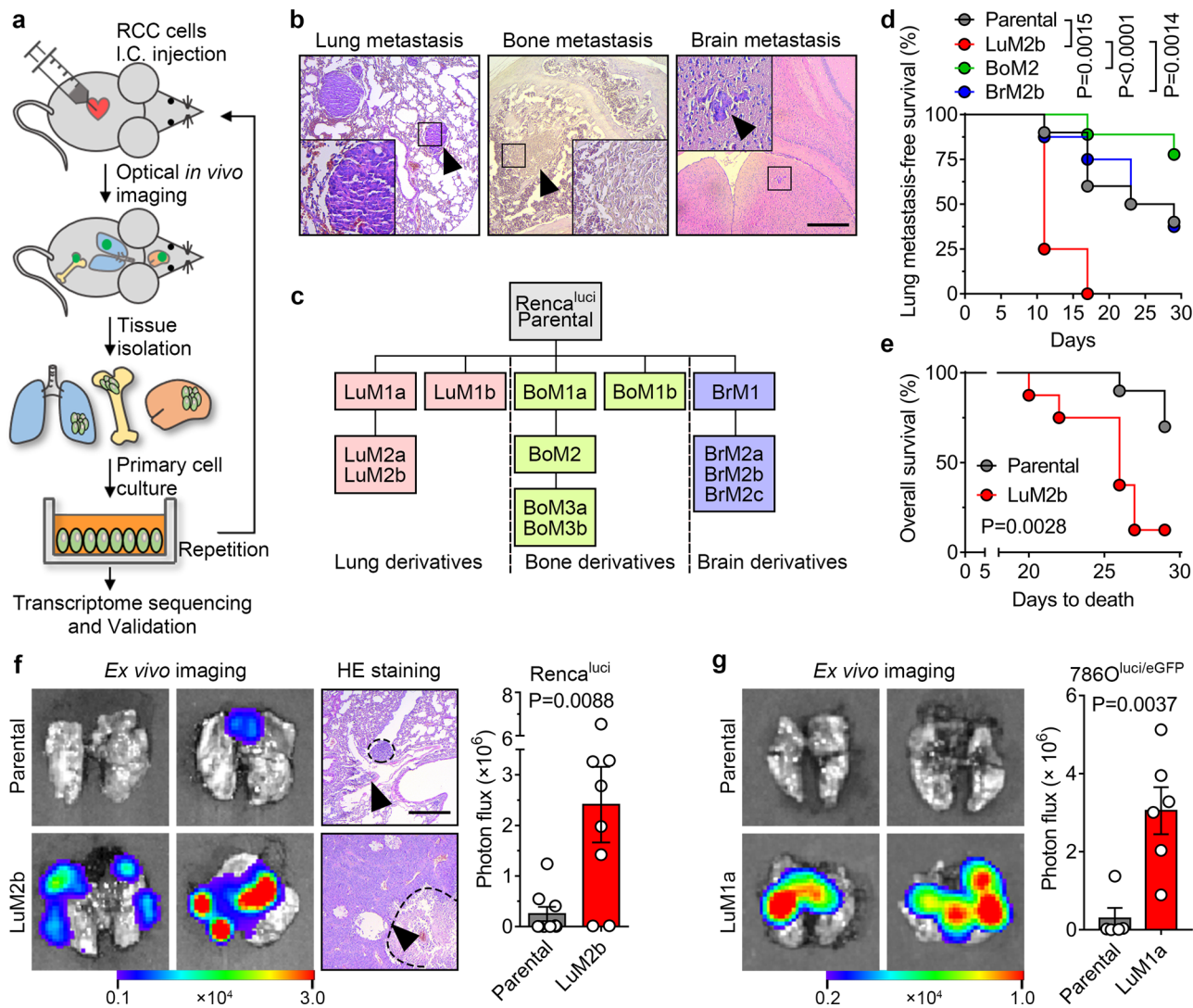


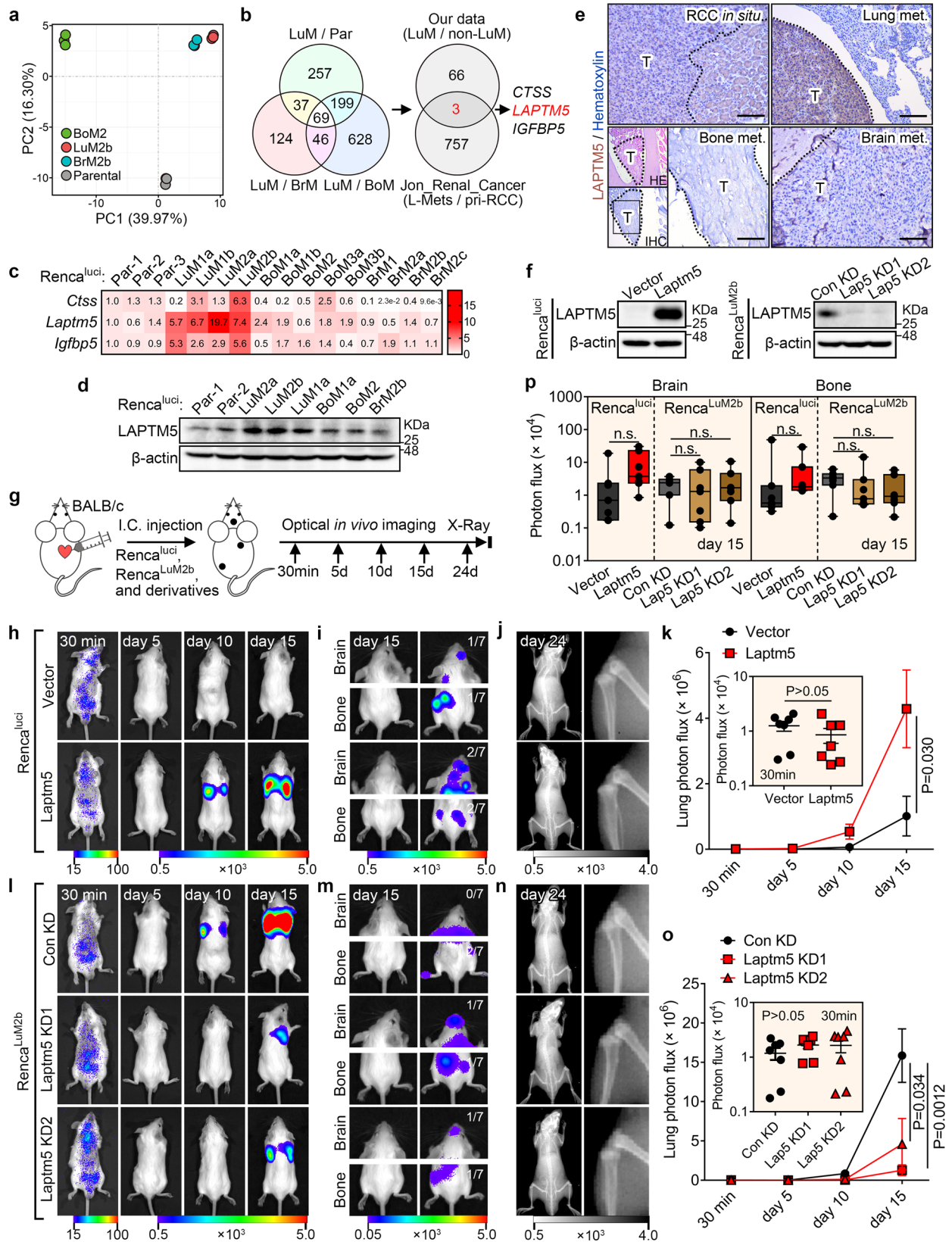
**Fig. 1** Isolation, characterization, and analysis of lung metastatic derivatives. **a** Construction of the multi-organ metastasis model and screening of organospecific metastatic cell derivatives. I.C., intracardiac. **b** Hematein-eosin (H&E) staining of lung, bone, and brain metastases (arrowheads) by Renca<sup>luci</sup> cells. Scale bar, 400  $\mu$ m. **c** Flowchart of the in vivo selection of lung, bone, and brain-specific metastatic subpopulations from Renca<sup>luci</sup> cells. **d** Kaplan-Meier survival curves for lung metastasis-free survival of Renca<sup>luci</sup> cells and representative derivatives (Parental,  $n = 10$  mice; LuM2b,  $n = 8$  mice; BoM2,  $n = 9$  mice; BrM2b,  $n = 8$  mice). **e** Kaplan-Meier survival curves for overall survival of Renca<sup>Parental</sup> and Renca<sup>LuM2b</sup> cells (Parental,  $n = 10$  mice; LuM2b,  $n = 8$  mice). **f** Representative ex vivo bioluminescent and H&E images of lung metastases at 30 days after I.C. injection of Renca<sup>luci</sup> cells (Parental,  $n = 9$  mice; LuM2b,  $n = 8$  mice; left panel) and quantification of the photon flux (right panel). Scale bar, 400  $\mu$ m. **g** Representative ex vivo bioluminescent images of lung metastases at 90 days after I.C. injection of 786O<sup>luci/eGFP</sup> cells (Parental,  $n = 5$  mice; LuM1a,  $n = 6$  mice; left panel) and quantification of the photon flux (right panel). In **f** and **g**, the data are presented as mean  $\pm$  SEM. Two-sided log-rank test was used for statistical analysis of (**d**) and (**e**), two-tailed Student's unpaired *t*-test for (**f**) and (**g**). Source data are provided as a Source data file.

To determine whether LAPT<sup>M5</sup> contributes to organotropic metastasis, we stably overexpressed *Laptm5* in Renca<sup>luci</sup> cells and knockdown *Laptm5* in Renca<sup>LuM2b</sup> cells, respectively (Fig. 2f), and tested their metastasis potential in vivo (Fig. 2g). Overexpression of *Laptm5* in Renca<sup>luci</sup> cells markedly accelerated lung metastasis (Fig. 2h, k), whereas knockdown of *Laptm5* in Renca<sup>LuM2b</sup> cells significantly suppressed lung metastasis (Fig. 2l, o). In contrast, the bone and brain metastasis ability of both Renca<sup>luci</sup> and Renca<sup>LuM2b</sup> cells were not affected by *Laptm5* expression levels (Fig. 2i, j, m, n, p). A parallel experiment carried out in the human RCC cell lines 786O<sup>Luci/eGFP</sup> and 786O<sup>LuM1a/786O<sup>LuM1b</sup></sup> also revealed similar roles of LAPT<sup>M5</sup> in mouse models of lung metastasis (Supplementary Fig. 3c–f). Moreover, ectopically expressed LAPT<sup>M5</sup> in Renca<sup>luci</sup> bone- and brain-derivatives converted their organotropism and enhanced their ability to metastasize to the lung (Supplementary

Fig. 3g, h). Together, these results established that LAPT<sup>M5</sup> is a positive regulator of renal cancer lung metastasis.

**LAPT<sup>M5</sup> promotes self-renewal and cancer stem cell-like traits of RCC cells.** Proliferation, epithelial-mesenchymal transition (EMT) plasticity, resistance to apoptosis, and self-renewal in foreign microenvironment are vital intrinsic properties of metastasizing tumor cells<sup>32,33</sup>. Therefore, we investigated the effect of LAPT<sup>M5</sup> on each of these cellular processes. Firstly, altering the expression of LAPT<sup>M5</sup> in RCC cells did not affect the in vitro proliferation rate (Supplementary Fig. 4a–c). Secondly, LAPT<sup>M5</sup> neither induced the EMT process nor enhanced the invasiveness of Renca cells or 786-O cells (Supplementary Fig. 4d, e). Thirdly, no notable apoptosis-resistance effect of LAPT<sup>M5</sup> in Renca<sup>luci</sup> cells was observed in vivo (Supplementary Fig. 4f). Lastly, to test





whether LAPTM5 is associated with self-renewal ability of cancer cells, we established the forced lung metastasis model by directly injecting Renca<sup>lucif</sup> and derivative cell lines into mouse tail vein and collected the lungs at different time points (Fig. 3a). IHC staining of luciferase in lung sections revealed that tumor cells extravasated in the stroma of the lung as early as one day after injection (Fig. 3b).

LAPTM5 overexpression did not enhance the ability of Renca<sup>lucif</sup> cells to infiltrate the lung (Supplementary Fig. 4g), but accelerated the formation of both micro-metastases (maximum diameter < 100 μm) and macro-metastases (maximum diameter > 100 μm) since day 7 (Fig. 3b–d). On the contrary, silencing of *Laptm5* suppressed the metastatic outgrowth of Renca<sup>LuM2b</sup> cells in the lung stroma



**Fig. 2 LAPTMS mediates lung-specific metastasis.** **a** Principal component analysis (PCA) of Renca<sup>luci</sup> parental and derivative cells. **b** Overlap of up-regulated genes in Renca<sup>LuM2b</sup> cells (LuM) as compared to Renca<sup>Parental</sup> (Par), Renca<sup>BrM2b</sup> (BrM) and Renca<sup>BoM2</sup> (BoM) cells (left panel) and further overlap with up-regulated genes in RCC lung metastases (L-Mets) as compared with primary RCC without lung metastases (pri-RCC) in the Jon\_Renal\_Cancer dataset (right panel). **c** Heatmap showing the mRNA expression of *Ctss*, *Laptm5* and *Igfbp5* in Renca<sup>luci</sup> parental and derivative cells measured by qRT-PCR, relative gene expression in each cell was compared with parental-1 (Par-1). **d** Immunoblotting (IB) analyses of LAPTMS expression in Renca<sup>luci</sup> parental and derivative cells. **e** Immunohistochemistry (IHC) analysis of LAPTMS staining in RCC in situ (renal subcapsular injection) and lung, bone, brain metastases. HE staining was used to show the site of bone metastasis. T, tumor. Scale bar, 200  $\mu$ m. **f** IB analysis of control and *Laptm5*-overexpressing Renca<sup>luci</sup> cells or control and *Laptm5*-silenced Renca<sup>LuM2b</sup> cells. **g** Schematic illustration for intracardiac cell inoculation and metastasis detection. Representative bioluminescent images of lung metastases (**h**), brain and bone metastases (**i**) in mice treated as in (**g**) with Renca<sup>luci</sup> and derivatives. **j** Representative X-ray images of bone metastases in mice treated as in (**g**). **k** Quantification of photon flux changes of lung metastases in (**h**) ( $n = 7$  mice per group). **l, m** Representative bioluminescent images of lung metastases (**l**), brain and bone metastases (**m**) in mice treated as in (**g**) with Renca<sup>LuM2b</sup> and derivatives. **n** Representative X-ray images of bone metastases in mice treated as in (**g**). **o** Quantification of photon flux changes of lung metastases in (L) ( $n = 7$  mice per group). **p** Quantification of photon flux of brain and bone metastases at 15 days after I.C. inoculation with indicated cells ( $n = 7$  mice per group). Boxes represent data within the 25th to 75th percentiles, n.s., not significant. Immunoblots are representative of three biological replicates. In **k** and **o**, the data are presented as mean  $\pm$  SEM, in (**p**), the data are presented as whisker plots: midline, median; box, 25–75th percentile; whisker, minimum to maximum values. Two-tailed Student's unpaired t-test were used for statistical analysis in all panels. Source data are provided as a Source data file.

(Supplementary Fig. 4g–j). We also exploited a doxycycline (Dox)-inducible (Tet-on) system to induce LAPTMS expression in Renca<sup>luci</sup> cells after extravasation in the lung (Supplementary Fig. 4k, l), LAPTMS also promoted the formation of metastases in the lung in the Tet-on system (Supplementary Fig. 4l–o), suggesting that LAPTMS may induce metastasis initiation and tumor outgrowth in the lung stroma.

Given the proposed connection between stemness and metastasis initiation<sup>7,8</sup>, we next investigated whether LAPTMS promotes lung metastasis by regulating cancer stem cell (CSC)-like traits of RCC cells. First, we performed the 3D tumor sphere formation assay and found that LAPTMS-overexpressing Renca or 786-O cells formed significantly more tumor spheres than the control cells while depletion of *Laptm5* suppressed the ability of Renca<sup>LuM2b</sup> cells to form tumor spheres (Fig. 3e, f and Supplementary Fig. 4p), indicating the involvement of LAPTMS in self-renewal. Next, we examined whether LAPTMS could enhance tumor initiation in vivo. As expected, LAPTMS overexpression significantly enhanced the subcutaneous tumor initiation ability of Renca cells in mice (Fig. 3g, h and Supplementary Fig. 5a). Conversely, silencing of *Laptm5* markedly inhibited the subcutaneous tumor initiation ability of Renca<sup>LuM2b</sup> cells (Fig. 3g, i and Supplementary Fig. 5a). Similarly, the tumor initiation ability of Renca cells in mouse renal subcapsular was also promoted by LAPTMS overexpression when limited cells were implanted (Supplementary Fig. 5b). Moreover, three of the four most common embryonic stem cell (ESC) transcription factors, *NANOG*, *OCT4*, *SOX2*, and *KLF4*, which are often reactivated in aggressive and metastatic RCC<sup>34</sup>, were significantly elevated in LAPTMS-overexpressed Renca and 786-O cells (Fig. 3j–k). Taken together, these results suggested that LAPTMS may promote and sustain stem cell-like traits in RCC cells.

**LAPTMS suppresses BMP signaling.** To explore the potential mechanism by which LAPTMS regulates the CSC traits and mediates lung-specific metastasis, we first performed gene set enrichment analysis (GSEA) in The Cancer Genome Atlas (TCGA) database for two major pathological types of RCC: clear-cell RCC (KIRC, 537 samples) and papillary RCC (KIRP, 291 samples). Since the majority of LAPTMS literature reported its negative regulation of membrane receptors<sup>35–37</sup>, we emphasized on signaling pathways that are suppressed by LAPTMS. We found that BMP signaling was the only pathway that exhibited a significantly negative correlation with LAPTMS levels in both KIRC and KIRP patients (Fig. 4a–c and Supplementary Data 3,

4). Intriguingly, bioactive BMP molecules from the lung stroma have been reported to inhibit the CSC traits of metastasis-initiating breast cancer cells circulating to the lung through phosphorylation of Smad 1/5/9 (Smad 1/5/8 in mice)<sup>13,38</sup>. Consistent with previous reports, we also detected high levels of Smad 1/5/8 phosphorylation in lung tissues, but not in the bone or brain tissue of Renca-bearing mice (Supplementary Fig. 6a). Hence, we focused on the BMP pathway. We first showed that recombinant murine BMP4 could induce the phosphorylation of Smad 1/5/8 in the parental Renca<sup>luci</sup> cells or the bone and brain derivatives but not the lung derivatives (Supplementary Fig. 6b and Fig. 4d). IHC analysis also confirmed the absence of Smad 1/5/8 phosphorylation in lung metastases by Renca<sup>luci</sup> (Fig. 4e). Based on these observations, we speculated that LAPTMS enables RCC cells to overcome the inhibitory effect of the lung-derived BMP anti-metastatic signal on CSC traits. To prove this hypothesis, we first showed that LAPTMS-overexpressing Renca cells exhibited reduced susceptibility to BMP4-induced Smad 1/5/8 phosphorylation (Fig. 4f). Consistently, depletion of *Laptm5* rescued the resistance to BMP4 in Renca<sup>LuM2b</sup> cells (Fig. 4f). Similarly, in 786-O cells, phosphorylation of Smad 1/5/9 was also significantly suppressed with ectopic LAPTMS expression upon stimulation with BMP4 (Supplementary Fig. 6c). Besides, we assessed the effect of LAPTMS on TGF- $\beta$  signaling, a pathway that interacts with BMP signals<sup>39</sup>. In 786-O and Renca cells, alteration of LAPTMS expression did not affect the stimulation of Smad pathways by TGF- $\beta$ 1 (Supplementary Fig. 6d). Moreover, treatment of Renca cells with 30 ng/mL BMP4 for 7 days markedly inhibited tumor sphere formation which was reversed by overexpression of LAPTMS (Fig. 4g). Conversely, treatment of Renca<sup>LuM2b</sup> cells with DMH1, a small molecule inhibitor of the BMP receptors, reversed the inhibitory effect of *Laptm5* knock-down on tumor sphere formation (Supplementary Fig. 6e and Fig. 4h), suggesting the function of LAPTMS was BMP-dependent. Furthermore, the mRNA levels of *Nanog*, *Oct4* and *Sox2* in Renca or 786-O cells were inhibited by BMP4 and rescued by LAPTMS expression (Fig. 4i and Supplementary Fig. 6f). Taken together, these data indicated that LAPTMS enhances the stem cell-like traits of RCC cells by suppressing the activation of BMP signaling in the lung microenvironment.

**LAPTMS downregulates BMPRIA at the post-transcriptional level.** It has been reported that BMPs, like other TGF- $\beta$  family members, elicit their effects through two types of serine-threonine kinase transmembrane receptors, type I and type II BMP receptors (BMPRs)<sup>39</sup>. Previous studies also suggested that LAPTMS

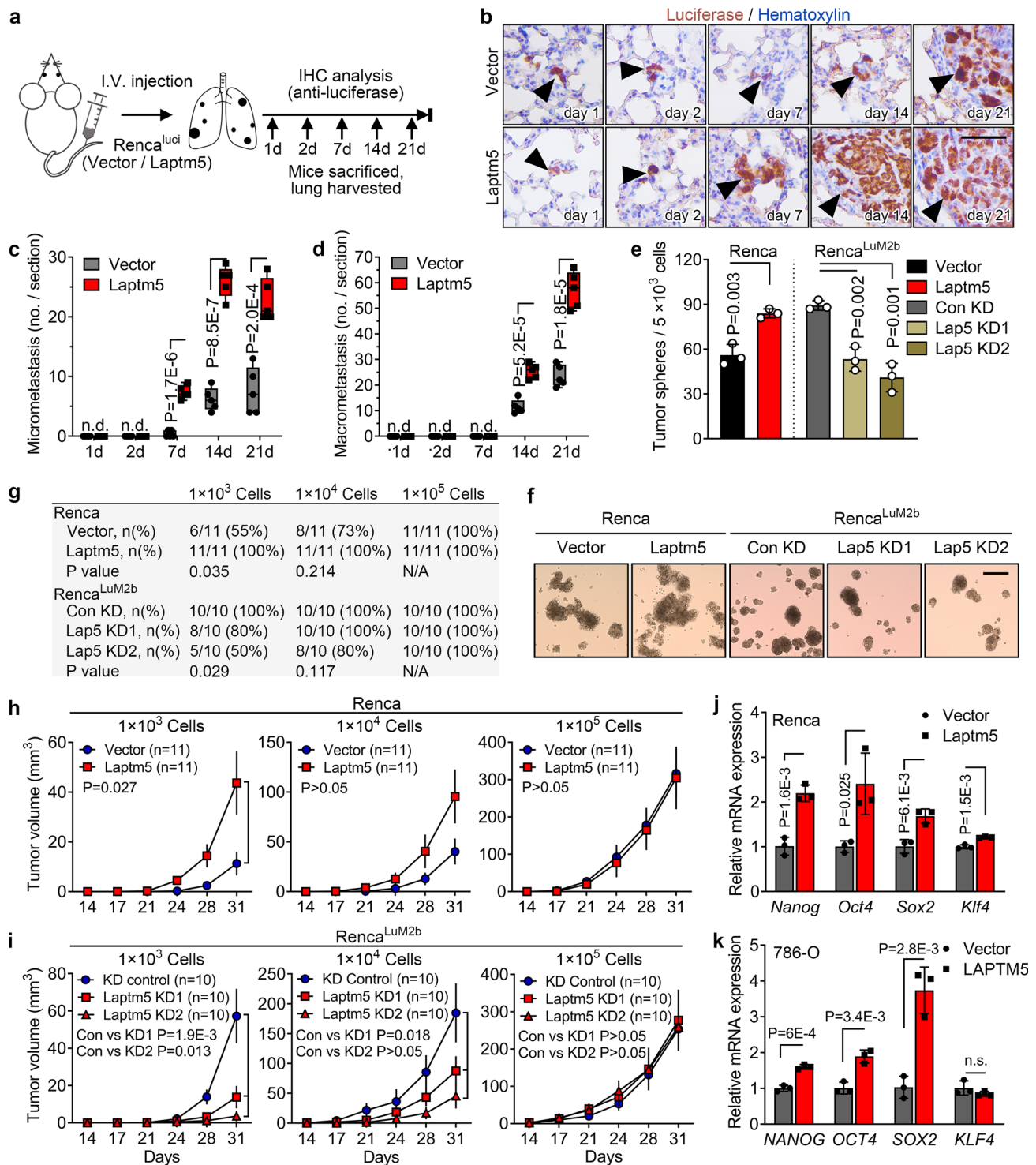
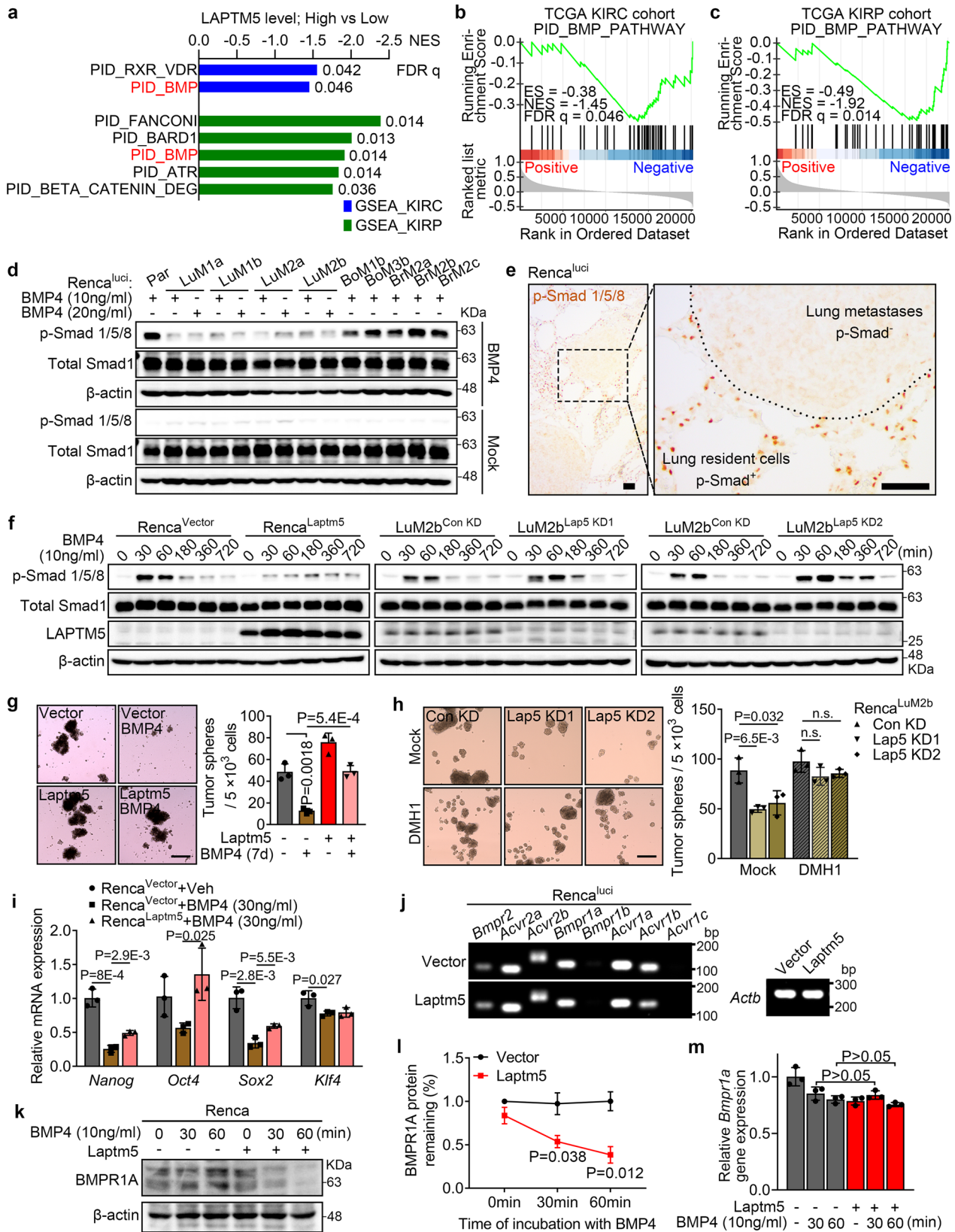


**Fig. 3** LAPTMS promotes self-renewal and cancer stem cell traits of RCC cells. **a** Schematic illustration for the steps of cell inoculation and lung metastases detection. I.V., intravenous. **b** Representative IHC images of luciferase staining in lung sections harvested from mice treated as in **(a)**. Scale bar, 50  $\mu$ m. Quantification of micrometastasis (diameter < 100  $\mu$ m, **c**) and macrometastasis (diameter  $\geq$  100  $\mu$ m, **d**) per lung section in **(b)** ( $n = 5$  mice per group). Tumor sphere assay (**e**) and quantification of tumor sphere formation of indicated cells (**f**,  $n = 3$  per group). Scale bar, 200  $\mu$ m. **g** Frequencies of tumors formation in indicated groups. Tumor volumes of control and Laptm5-overexpressing Renca cells (**h**,  $n = 11$  mice per group) or control and Laptm5-silenced Renca<sup>LuM2b</sup> cells (**i**,  $n = 10$  mice per group) inoculated subcutaneously with indicated cell number. **j**, **k** qRT-PCR analysis of stemness markers in control and LAPTMS-overexpressing Renca (**j**) and 786-O cells (**k**).  $n = 3$  per group. In **c**, **d**, the data are presented as whisker plots: midline, median; box, 25–75th percentile; whisker, minimum to maximum values, in **(e)**, **(j)**, and **(k)**, the data are presents as mean  $\pm$  SD, in **(h)** and **(i)**, the data are presents as mean  $\pm$  SEM. Two-tailed Student's unpaired  $t$ -test was used for statistical analysis in **(c)**–**(e)**, **(h)**–**(k)**,  $\chi^2$  test for **(g)**. Source data are provided as a Source data file.



could regulate certain membrane receptor levels to modulate the response of cells to external stimuli<sup>35,36</sup>. Hence, we asked whether LAPTM5 could regulate BMPRs in RCC cells. We first identified the types of BMPRs expressed in RCC cells. Semiquantitative RT-PCR showed that all major known BMPRs except *Bmpr1b* and *Acvr1c* were expressed in Renca cells (Fig. 4j), and that the

transcriptional levels of these BMPRs were not affected by LAPTM5 manipulation (Fig. 4j and Supplementary Fig. 6g). However, upon treatment with 10 ng/mL murine BMP4, the protein level of one of the BMPRs, BMPR1A, gradually decreased over time in LAPTM5-overexpressing Renca cells but not in control cells, while the mRNA level of *Bmpr1a* was not affected



**Fig. 4 LAPTMS blocks BMP signal and negatively regulates BMPRIA.** **a** Differentially expressed cancer-related gene sets (C2\_PATHWAYS) with high LAPTMS expression in the TCGA KIRC cohort and KIRP cohort (Top 5). NES, normalized enrichment score. FDR  $q$ , false discovery rate  $q$  value. GSEA output of genes in the PID\_BMP\_Pathway by LAPTMS high and low expression groups from the KIRC cohort (**b**) and KIRP cohort (**c**) in the TCGA database. ES, enrichment score. **d** IB analysis of Renca<sup>luci</sup> parental and derivative cells treated with Mock (ddH<sub>2</sub>O), or recombinant murine BMP4 (10 ng/mL or 20 ng/mL) for 60 min. **e** IHC analysis of p-Smad 1/5/8 levels in lung metastases of Renca<sup>luci</sup>. Scale bar, 50  $\mu$ m. **f** IB analysis of control and Laptm5-overexpressing Renca cells (left panel) or control and Laptm5-silenced Renca<sup>LuM2b</sup> cells (middle and right panel) treated with BMP4 (10 ng/mL) for indicated times. **g** Representative images of tumor sphere assay of control and Laptm5-overexpressing Renca cells treated with or without BMP4 (30 ng/mL) for 7 days, and quantification of tumor sphere formation of indicated groups ( $n = 3$  per group). Scale bar, 200  $\mu$ m. **h** Representative images of tumor sphere assay of control and Laptm5-silenced Renca<sup>LuM2b</sup> cells treated with or without DMH1 (5  $\mu$ M) for 7 days, and quantification of tumor sphere formation of indicated groups ( $n = 3$  per group). Scale bar, 200  $\mu$ m. **i** qRT-PCR analysis of stemness markers in indicated cells.  $n = 3$  per group. **j** Semiquantitative RT-PCR analysis of BMP receptors in control and Laptm5-overexpressing Renca<sup>luci</sup> cells with *Actb* as control. **k** IB analysis of BMPRIA in control and Laptm5-overexpressing Renca cells treated with BMP4 (10 ng/mL) for indicated times. **l** Ratio of BMPRIA protein remaining in control and Laptm5-overexpressing Renca cells treated as in (**k**) ( $n = 3$  per group). **m** qRT-PCR analysis of *Bmpr1a* in control and Laptm5-overexpressing Renca cells treated with BMP4 (10 ng/mL) for indicated times.  $n = 3$  per group. Immunoblots are representative of three biological replicates. Data in bar graphs are presented as mean  $\pm$  SD. Two-tailed Student's unpaired  $t$ -test were used for statistical analysis in all panels. Source data are provided as a Source data file.

(Fig. 4k–m and Supplementary Fig. 6h, i). Correspondingly, BMPRIA protein level was upregulated in *Laptm5*-silenced Renca<sup>LuM2b</sup> cells (Supplementary Fig. 6j). Similarly, LAPTMS-overexpressing 786-O cells also showed a decrease in BMPRIA protein level but not mRNA level 60 min after BMP4 treatment (Supplementary Fig. 6k, l). Together, these data suggested that LAPTMS negatively regulated BMPRIA via post-transcriptional mechanisms in RCC cells.

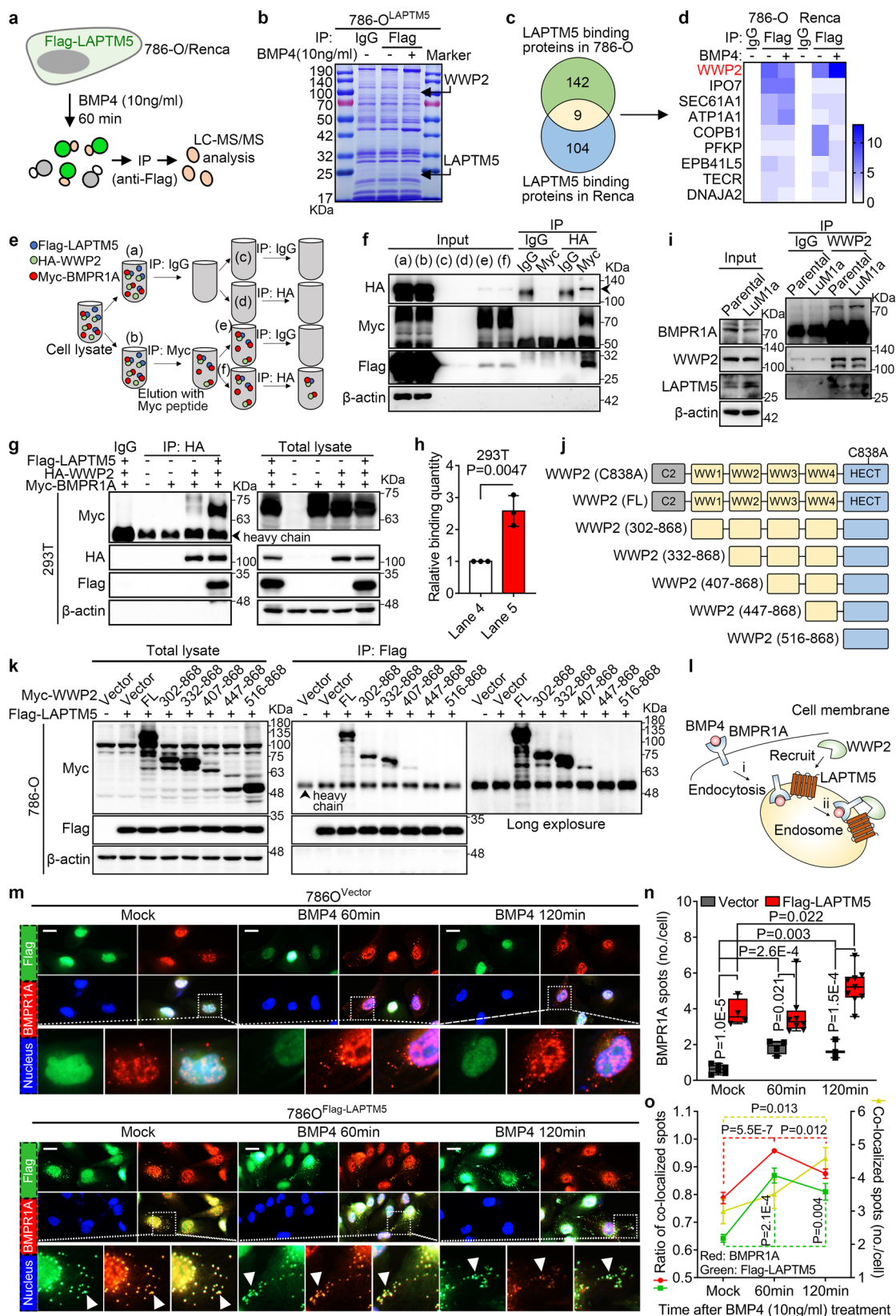
**LAPTMS promotes BMPRIA lysosomal sorting and binding with WWP2.** To investigate how LAPTMS mediates the down-regulation of BMPRIA protein, we stably overexpressed Flag-tagged LAPTMS in 786-O and Renca cells, respectively. Proteins that could interact with LAPTMS were then identified using IP-MS. After treatment with 10 ng/mL BMP4 for 60 min, LAPTMS-binding proteins were immunoprecipitated with Flag antibody and subjected to LC-MS/MS analysis (Fig. 5a, b and Supplementary Fig. 7a). A total of 151 and 113 proteins were identified in 786-O and Renca cells, respectively; of which 9 proteins were common in both lines, WW domain-containing E3 ubiquitin protein ligase 2 (WWP2, also called AIP2), a member of the NEDD4 protein family, ranked among the top of the list as a protein that might interact with LAPTMS (Fig. 5b–d and Supplementary Fig. 7a). Co-immunoprecipitation experiments confirmed the interaction between LAPTMS and WWP2 in both 786-O and Renca cells, which was further enhanced upon BMP4 treatment (Supplementary Fig. 7b, c). To determine if other NEDD4 family members also bind to LAPTMS, we carried out immunoprecipitation assays in LAPTMS-overexpressing 786-O or Renca cells and found that WWP2 was the only NEDD4 family protein that can bind to LAPTMS (Supplementary Fig. 7d). Moreover, the interaction between LAPTMS and WWP2 was also confirmed by immunofluorescence experiments (Supplementary Fig. 7e). NEDD4 family proteins, including SMURF1 and NEDD4L, have been shown to promote the endocytosis and/or ubiquitin-mediated degradation of membrane proteins<sup>40,41</sup>. To investigate whether LAPTMS promotes BMPRIA degradation via WWP2, we ectopically expressed Myc-tagged BMPRIA and Flag-tagged LAPTMS or HA-tagged WWP2 in 786-O cells, immunoprecipitation assays showed that BMPRIA receptor bound to both LAPTMS and WWP2, the binding was enhanced by BMP4 treatment, and the total BMPRIA protein level was reduced in the presence of LAPTMS or WWP2 (Supplementary Fig. 7f, g). Evidence of co-localization between WWP2 and BMPRIA was also provided by immunofluorescence assays in 786-O cells (Supplementary Fig. 7h). In addition, we performed serial IP experiments (Myc-BMPRIA pulldown followed by HA-WWP2 pulldown) and successfully detected the Flag-LAPTMS signal,

further proving that LAPTMS-WWP2-BMPRIA were in the same protein complex (Fig. 5e, f). Furthermore, when all three constructs were co-transfected in 293T cells or 786-O cells, LAPTMS dramatically promoted the interaction between WWP2 and BMPRIA (Fig. 5g, h and Supplementary Fig. 7i), suggesting a crucial regulatory role of LAPTMS in BMPRIA-WWP2 interaction. Likewise, endogenous interactions between LAPTMS-WWP2 and WWP2-BMPRIA were also confirmed in parental 786O<sup>luci/eGFP</sup> and the lung-met derivative 786O<sup>LuM1a</sup> cells (Fig. 5i).

WWP2 belongs to the NEDD4 family of E3 ubiquitin ligases that contains a conserved amino-terminal C2 domain, a variable number of WW domains, and a carboxy-terminal HECT domain<sup>42</sup>. To find out the specific binding sites between WWP2 and LAPTMS, we performed immunoprecipitation assays using either the full-length WWP2 construct or mutant WWP2 constructs lacking various functional domains (Fig. 5j), and found that all constructs shorter than 407–868 failed to bind with LAPTMS, suggesting that the C2 domain and the first two and the last WW domains are dispensable for LAPTMS binding, whereas the WW3 domain is required (Fig. 5k).

It was reported that ectopically expressed LAPTMS mainly localizes to late endosomes and/or lysosomes<sup>43,44</sup>. In RCC cells, we confirmed that endogenous LAPTMS mostly co-localizes with the late endosome and/or lysosome makers LAMP1 and RAB7, but not with early endosome markers EEA1 and RAB5<sup>45</sup> (Supplementary Fig. 7j). Using immunofluorescence, we observed that LAPTMS facilitated BMPRIA endocytosis in untreated and BMP4-treated 786-O cells. Moreover, BMP4 treatment induced a more dramatic increase in BMPRIA endocytosis in LAPTMS-overexpressing cells compared to control cells (Fig. 5l–n). In addition, BMPRIA and LAPTMS displayed the most co-localization (Fig. 5m, o, green and red lines, respectively), and BMP4 treatment enhanced the co-localization signal (Fig. 5m, o, yellow line), further confirming the previous immunoprecipitation results. Similarly, in lung metastatic 786O<sup>LuM1a</sup> cells, we also observed an increase in the late endosome and/or lysosome formed by LAPTMS, as well as an increase in BMPRIA endocytosis, which was further enhanced by BMP4 treatment (Supplementary Fig. 7k). Taken together, these data demonstrated that LAPTMS facilitates the endocytosis of BMPRIA and its interaction with WWP2.

**WWP2 mediates lysosome-based ubiquitination and degradation of BMPRIA.** It is well established that ubiquitination of membrane receptors is required for lysosome-mediated degradation, we, therefore, investigated whether WWP2 ubiquitylates BMPRIA. In 293T cells, the conjugation of ubiquitin chains to



BMPR1A was markedly increased in the presence of WWP2, and further increased by the co-expression of LAPTMs5 (Supplementary Fig. 8a), suggesting that LAPTMs5 promoted the interaction between WWP2 and BMPR1A. The ubiquitination of BMPR1A by WWP2 was also confirmed in the RCC cell line 786-O (Fig. 6a). In both 293T and 786-O cells, BMPR1A

ubiquitination was inhibited by the expression of a catalytically inactive mutant of WWP2 (WWP2<sup>C838A</sup>)<sup>46</sup> (Fig. 6b and Supplementary Fig. 8b). Moreover, silencing of WWP2 with three different small interfering RNAs (siRNA) also reduced BMPR1A ubiquitination (Fig. 6c and Supplementary Fig. 8c). Furthermore, treatment of 293T cells co-expressing LAPTMs5 and

**Fig. 5 LAPTMS directly interacts with WWP2 and promotes BMPR1A lysosomal sorting.** **a** Schematic illustration of TMT-labeled LC-MS/MS analysis in 786O<sup>LAPTMS</sup> and Renca<sup>Lap<sup>tm5</sup></sup> cells treated or untreated with BMP4 (10 ng/mL) for 60 min. **b** Coomassie brilliant blue staining of 786O<sup>LAPTMS</sup> cells treated or untreated with BMP4 (10 ng/mL) for 60 min. The arrowheads indicate bands of WWP2 and LAPTMS, respectively. **c** Overlap of identified LAPTMS-binding proteins in 786O<sup>LAPTMS</sup> and Renca<sup>Lap<sup>tm5</sup></sup> cells. **d** Heatmap of the nine proteins identified binding to LAPTMS by TMT-labeled LC-MS/MS analysis. Schematic illustration (**e**) and IB result (**f**) of serial immunoprecipitation (IP) analysis using anti-Myc (first round) and anti-HA (second round) in 293T cells transfected with expression vectors for Flag-LAPTMS, HA-WWP2, and Myc-BMPR1A. Arrowhead indicates the band of HA-WWP2. **g** IP and IB analyses of 293T cells transfected with expression vectors for Flag-LAPTMS, HA-WWP2, and Myc-BMPR1A. **h** Quantitation of the binding between HA-WWP2 and Myc-BMPR1A as treated in (**g**) ( $n = 3$  per group). **i** IP and IB analyses of 786O<sup>Luci/eGFP</sup> Parental and LuM1a cells. **j** Schematic illustration of full-length (FL) WWP2 and its deletion mutants lacking functional domains (ranges indicate amino acids present in construct). C838A represents the mutation of cytosine to adenine in the 838th nucleotide. **k** IP and IB analyses of 786-O cells transfected with expression vector for Flag-LAPTMS, control (Vector) or Myc-tagged full-length WWP2 or various deletion mutants. **l** Schematic illustration of LAPTMS, WWP2 and BMPR1A interactions in cells. **m** Immunofluorescence (IF) analysis of control (upper panel) and LAPTMS-overexpressing (lower panel) 786-O cells treated with Mock (ddH<sub>2</sub>O), or BMP4 (10 ng/mL) for 60 min or 120 min. Scale bar, 10  $\mu$ m. **n** Quantification of BMPR1A punctate spots per 786-O cell treated as in (**m**) [ $n =$  biological replicates, 6 in Vector, 4 in LAPTMS (Mock);  $n = 4$  in Vector, 8 in LAPTMS (60 min);  $n = 3$  in Vector, 9 in LAPTMS (120 min)]. Data are presented as whisker plots: midline, median; box, 25–75th percentile; whisker, minimum to maximum values. **o** Ratio of co-localized spots to total BMPR1A (red line) or LAPTMS (green line) spots and quantification of co-localized spots per 786-O cell (yellow line) treated as in (**m**) ( $n = 4, 8, 9$  biological replicates in group Mock, 60 min, 120 min, respectively). Immunoblots are representative of three biological replicates. Data are presented as mean  $\pm$  SD in (**h**), and mean  $\pm$  SEM in (**o**). Two-tailed Student's unpaired  $t$ -test was used for statistical analysis in all panels. Source data are provided as a Source data file.

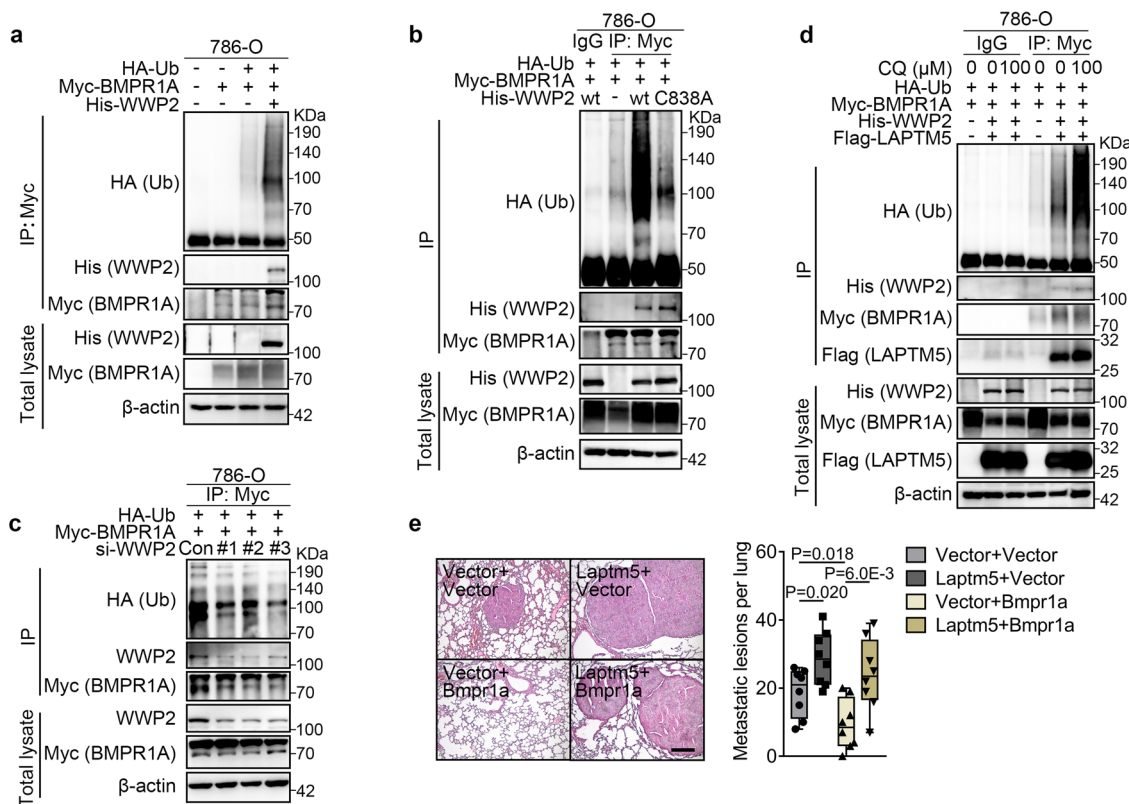


**Fig. 6 WWP2 promotes lysosome-based polyubiquitylation and degradation of BMPR1A.** **a** IP and IB analyses of 786-O cells transfected with expression vectors for His-WWP2, Myc-BMPR1A and HA-ubiquitin (Ub). **b** IP and IB analyses of 786-O cells transfected with expression vectors for His-tagged wild type (wt) or C838A mutated WWP2, Myc-BMPR1A and HA-Ub. **c** IP and IB analyses of 786-O cells transfected with siRNAs against WWP2 or expression vectors for Myc-BMPR1A and HA-Ub. **d** IP and IB analyses of 786-O cells transfected with expression vectors for Flag-LAPTMS, His-WWP2, Myc-BMPR1A, HA-Ub and treated with different concentrations of chloroquine (CQ) for 60 min. **e** Representative H&E images of lung metastases at 21 days after I.V. injection of Renca cells stably expressing Laptm5 and/or Bmpr1a (left panel) and quantification of the lung metastatic lesions per slide (right panel,  $n = 8$  mice per group). Data are presented as whisker plots: midline, median; box, 25–75th percentile; whisker, minimum to maximum values. Two-tailed Student's unpaired  $t$ -test was used for statistical analysis. Immunoblots are representative of three biological replicates. Source data are provided as a Source data file.

WWP2 with the lysosome inhibitor chloroquine diphosphate (CQ) resulted in a dose-dependent increase in both BMPR1A ubiquitination and total BMPR1A protein levels (Fig. 6d and Supplementary Fig. 8d), supporting that LAPTMS-based lysosome pathway promoted the degradation of ubiquitinated BMPR1A. Lastly, in the *in vivo* lung metastasis assay using

Renca cells, the metastatic suppressor role of ectopically expressed BMPR1A was reversed by LAPTMS co-expression (Fig. 6e). Taken together, these data revealed that WWP2 facilitated BMPR1A polyubiquitination and that the LAPTMS/WWP2-based lysosome pathway mediated the integrated process of BMPR1A degradation.



**LAPTM5 negatively correlates with BMPR1A in clinical RCC specimens and predicts lung metastasis.** To study the expression patterns of LAPTM5 and BMPR1A in clinical samples, we gathered a cohort of 34 RCC metastases from the lung, bone, and brain, as well as 106 normal kidney tissues and 150 primary RCC tissues and performed IHC analysis for both LAPTM5 and BMPR1A. LAPTM5 displayed remarkably higher expression levels in lung metastases than in bone ( $P < 0.001$ ) and brain metastases ( $P = 0.039$ ), and primary RCC tissues ( $P < 0.0001$ ) (Fig. 7a, b). We also confirmed that neither bone nor brain metastases showed divergent expression of LAPTM5 compared with primary tumors (Fig. 7a, b). More importantly, BMPR1A expression levels were lower in lung metastases than in other organ metastases (Fig. 7c and Supplementary Fig. 9a). Quantitation of LAPTM5 and BMPR1A expression levels showed a tight negative correlation pattern in RCC metastases ( $R = -0.459$ ,  $P = 0.006$ ) (Fig. 7d).

To evaluate the relationship between LAPTM5 and BMPR1A expression in primary RCC tumors, we collected and analyzed clinical information from patients with primary RCC tumors. Histological staining showed that LAPTM5 was upregulated in RCC tissues compared with normal kidney tissues ( $P < 0.0001$ ) (Fig. 7a, b). Besides, staining of two consecutive tissue sections with either LAPTM5 or BMPR1A antibody showed high regional LAPTM5 expression in most primary RCC tissues, as well as a negative correlation between LAPTM5 and BMPR1A expression (Supplementary Fig. 9b, c), which is similar to that observed in RCC metastases. Moreover, statistical analysis revealed a significant correlation between the staining intensity of LAPTM5 and histological grade ( $P = 0.039$ ), TNM stage ( $P = 0.038$ ), adverse pathological events ( $P = 0.002$ ) and distant metastasis ( $P < 0.001$ ) of primary RCC (Supplementary Fig. 9d and Supplementary Data 5). In addition, primary RCC tissues of patients with lung metastases displayed higher LAPTM5 levels than those without lung metastases but lower LAPTM5 levels than lung metastases tissues (Fig. 7e and Supplementary Fig. 9e). To further assess the predictive value of LAPTM5 expression for RCC lung metastasis, we performed univariate and multivariable logistic regression analyses. The results revealed that LAPTM5 expression, like the histological grade, was an independent predictor of lung metastasis in RCC ( $P < 0.001$ ) (Fig. 7f). Furthermore, reduced metastatic-free survival (MFS) and overall survival (OS) were found in RCC patients with high LAPTM5 expression in primary tumors (Fig. 7g, h). These clinical data confirmed the negative correlation between LAPTM5 and BMPR1A as depicted in the schematic (Fig. 7i). LAPTM5 expression levels may thus serve as an independent prognosis factor of lung metastasis and survival of RCC patients.

**LAPTM5 is specifically activated in lung metastasis of multiple cancers.** To extend our findings to other cancer types, we analyzed the transcriptional profile of a set of breast cancer cell lines generated by in vivo organotropic metastatic clone selection<sup>19</sup> (Fig. 8a). In this dataset, LAPTM5 also exhibited higher levels in breast cancer cells with high lung-specific metastatic activity (Lung-M) than in those with mediate activity (Mediate) and bone-specific metastatic activity (Bone-M) (Fig. 8b). Similarly, when we examined LAPTM5 expression in a melanoma dataset (GSE50496) and a colorectal cancer dataset (GSE41258), higher levels of LAPTM5 were also found in lung metastases than other organ metastases<sup>47,48</sup> (Fig. 8c, d).

In agreement with the findings in RCC cells, overexpression of LAPTM5 promoted the sphere formation ability of the murine 4T1<sup>luci</sup> and human MDA-MB-231 breast cancer cell lines in vitro while silencing of *Laptm5* suppressed sphere formation (Fig. 8e and Supplementary Fig. 10a–d). LAPTM5 also increased the ability of

4T1<sup>luci</sup> cells to form orthotopic tumors in vivo when implanted into the mammary glands of mice (Fig. 8f, g and Supplementary Fig. 10e, f). More importantly, under the condition ( $1 \times 10^5$  cells) where no difference in primary tumor formation rate was observed (Fig. 8g and Supplementary Fig. 10e, f), LAPTM5 overexpression resulted in increased metastatic lesion-forming activity in the lung, and *Laptm5* knockdown significantly inhibited lung metastasis (Fig. 8f, h, i).

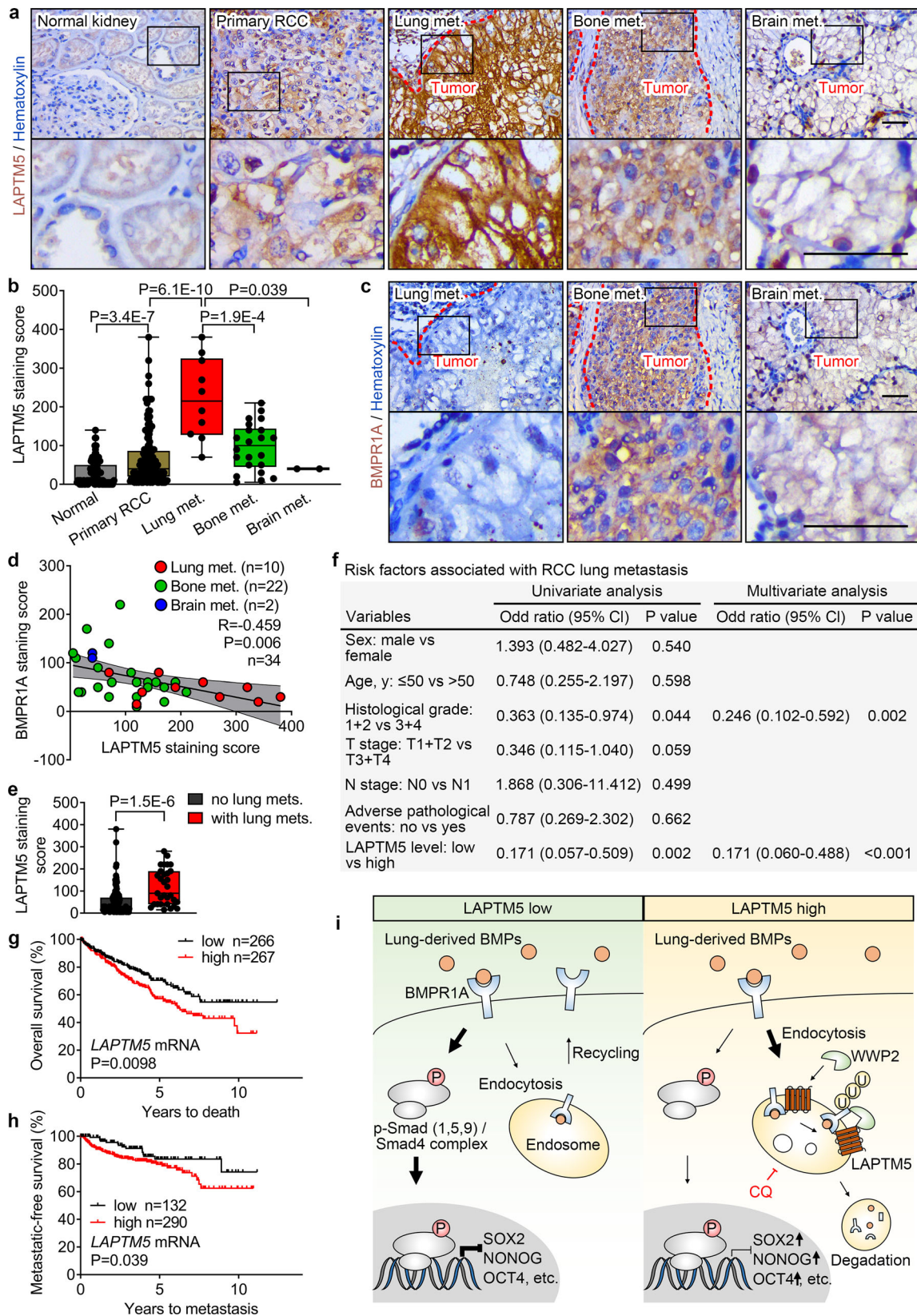
Next, we examined whether LAPTM5 affected the response of breast cancer cells to BMP stimulation. Immunoblotting results showed that LAPTM5 silencing accelerated the phosphorylation of Smad 1/5/9 in MDA-MB-231 cells in response to BMP4 treatment (Supplementary Fig. 10g). Immunoprecipitation assay also confirmed the interaction between LAPTM5 and WWP2 in 4T1<sup>luci</sup> cells; which was enhanced in the presence of BMP4 (Supplementary Fig. 10h). LAPTM5 and BMPR1A also exhibited co-localization in MDA-MB-231<sup>LAPTM5</sup> cells (Supplementary Fig. 10i). After pretreatment with 10 ng/mL BMP4 for 60 or 120 min, the punctate spots formed by BMPR1A in cells increased significantly and LAPTM5 overexpression promoted the endocytosis of BMPR1A in MDA-MB-231 cells (Supplementary Fig. 10j, k). Moreover, WWP2 was also found to bind to BMPR1A and promote its degradation in MDA-MB-231 cells (Supplementary Fig. 10l).

In conclusion, these data demonstrated that the activation of LAPTM5 in lung metastases is a common molecular event shared by several types of human cancer, and that the LAPTM5/WWP2-based lysosomal regulatory pathway mediates the ubiquitination and degradation of BMPR1A.

## Discussion

Organ specificity observed in cancer metastasis is known as organotropism and remains one of the most intriguing and unanswered questions in cancer biology. With regard to lung-specific metastasis, limited but essential efforts have been devoted to breast cancer and only a few groundbreaking discoveries have been made<sup>13,19,38</sup>. However, related research on RCC has not yet been reported. Here, we document a critical role of LAPTM5, which regulates the self-renewal and cancer stem cell-like traits of RCC cells in lung stroma, thus promoting lung-specific metastasis of RCC.

By integrated analyses of transcriptional profiles in clinical samples and Renca<sup>luci</sup> RCC cell line derivatives with distinct organ metastasis tendency, we showed that LAPTM5 was preferentially activated in lung metastasis and was required for RCC cells to develop lung-specific metastases. Phenotypically, we founded that LAPTM5 contributed to the self-renewal and cancer stem cell-like traits of RCC cells in lung stroma by blocking the effect of lung stroma-derived BMPs. Mechanistic studies using IP-MS in murine and human RCC cell lines (Renca and 786-O) uncovered aLAPTM5 binding protein WWP2 and established the regulatory role of LAPTM5/WWP2 in the ubiquitination and lysosomal degradation of BMPR1A. Furthermore, in primary and metastatic RCC clinical samples, we showed that LAPTM5 negatively correlated with BMPR1A levels and predicted lung metastatic frequency in renal cancer. Most importantly, activation of LAPTM5 in lung metastasis is a common molecular event shared by several types of cancer types. Another possibility that was not investigated in the current study is the tight correlation between LAPTM5 and immune-related or chemotactic pathways, like T/B cell antigen receptor (TCR/BCR)- and interleukin (IL)-associated pathways, in RCC. LAPTM5 has been reported to negatively regulate cell surface TCR/BCR expression via promoting their degradation in the lysosomal compartments to mediate T and B lymphocyte inactivation<sup>35,36</sup>. Moreover,



LAPT5 may be involved in regulating the immune micro-environment in KIRC<sup>49</sup>. Whether LAPT5 could also mediate lung-specific metastasis by regulating infiltrated immune cell function in primary or metastatic foci warrants further investigation.

Controversial roles of BMPs in organotrophic metastasis have been reported. For example, one study found that blocking BMP signal could lead to lung-specific metastasis in breast cancer<sup>13</sup>, while another study indicated that BMP signaling enhances bone metastasis of breast cancer through the Smad pathway<sup>50</sup>.



**Fig. 7 LAPT5 negatively correlates with BMP1A and predicts lung metastasis of RCC.** **a** Representative IHC images for LAPT5 in clinical sections of normal kidney tissue, primary RCC tissue, lung metastases (Lung met.), bone metastases (Bone met.) and brain metastases (Brain met.) from RCC patients. Scale bar, 100  $\mu$ m. **b** IHC staining score of LAPT5 in clinical primary RCC and organ metastases from RCC patients. Normal,  $n = 106$  samples; Primary RCC,  $n = 150$  samples; Lung met.,  $n = 10$  samples; Bone met.,  $n = 22$  samples; Brain met.,  $n = 2$  samples. **c** IHC images for BMP1A in clinical sections [Serial section of (a)] of lung metastases (Lung met.), bone metastases (Bone met.) and brain metastases (Brain met.) from RCC patients. Scale bar, 100  $\mu$ m. **d** Pearson correlation between LAPT5 and BMP1A levels in clinical RCC metastases.  $R$ , Pearson correlation coefficient; center line, mean of best-fit line; the shadow indicates 95% confidence interval. **e** IHC staining score of LAPT5 in primary RCC patients with lung metastases (with lung met.,  $n = 31$  samples) and those without lung metastases (no lung met.,  $n = 119$  samples). **f** Univariate and multivariate analyses to determine risk factors associated with lung metastasis of RCC patients ( $n = 150$  patients). CI: confidence interval. Kaplan–Meier survival curves for overall survival (**g**) and metastatic-free survival (**h**) of patients with low and high LAPT5 mRNA level in the TCGA KIRC cohort. **i** Schematic illustration of LAPT5 promoting lung-specific metastasis of RCC. CQ, chloroquine; P, phosphorylated; U, ubiquitylated. In **b** and **e**, the data are presented as whisker plots: midline, median; box, 25–75th percentile; whisker, minimum to maximum values. Two-tailed Student’s unpaired  $t$ -test in (**b**) and (**e**). Source data are provided as a Source data file.

We reasoned that BMPs play different roles in different tissues and that each organ uses distinct signaling molecules to suppress cancer metastasis. Thus, although BMPs are also present in the bone microenvironment because of its essential role in bone development and turnover<sup>39,51,52</sup>, it appears not to be used by the bone to suppress metastatic colonization of circulating tumor cells. In contrast, the lung tissues, at least in our models, exhibited much higher expression of BMPs, which appears to be the dominant signal used by the lung stroma to suppress the outgrowth of metastatic tumor cells. Moreover, our data also suggest that this metastasis suppressor role of BMP in the lung is not confined to renal cancer but a common molecular event shared by several types of human cancer.

The metastasis process involves the evolution, dissemination, and subsequent colonization and exit from dormancy of cancer cells from a primary tumor to a distant organ<sup>32,53</sup>. Elevated LAPT5 expression in lung metastases may occur at every phase of metastasis. According to our finding that higher LAPT5 levels were found in primary RCC tissues with lung metastases than in those without lung metastases, we inferred that LAPT5 is upregulated in primary tumors and is responsible for the initiation of lung metastasis. However, unlike in the *Jon\_Renal\_Cancer* dataset<sup>30</sup>, we detected even higher LAPT5 levels in the lung metastases tissues than primary tumor tissues in patients with lung metastases (Supplementary Fig. 9e); besides, LAPT5 level was increased after TGF- $\beta$  treatment<sup>54</sup>, therefore, whether the lung indigenous TGF- $\beta$ -rich environmental causes the upregulation of LAPT5 remains to be confirmed. In favor of the former hypothesis, most tumor cells in primary lesions did not show homogeneous LAPT5 expression, but exhibited regionally high LAPT5 expression<sup>26</sup>. However, the mechanisms underlying LAPT5 activation in these cells remain unexplored.

After the surgical resection of primary tumors, 17.5–21% RCC patients develop local recurrence or distant metastases with the lung being the preferred organ<sup>55,56</sup>. Histological analysis of LAPT5 in postoperative tissues, as revealed in this work, might serve as a predictor of lung metastasis in RCC patients and be helpful for follow-up plans and treatment decisions. More importantly, the insights from this work suggest a different translational strategy. Lysosome inhibitors, including CQ, hydroxychloroquine (HCQ), and its novel derivatives ROC325 and Lys05, either alone or in combination therapy, have shown excellent anti-tumor activity in preclinical models<sup>57–62</sup>. Although in previous clinical trials, the therapeutic effects of most lysosome inhibitors were disappointing against various cancers such as pancreatic cancer, colon cancer, glioma, and breast cancer<sup>63–67</sup>, the potent effect of CQ in blocking LAPT5 and restoring BMP1A levels makes it a promising therapeutic agent for patients with lung metastasis. Development of specific small-molecule inhibitors for LAPT5 is also needed. Moreover,

lysosomal autophagy participates in sunitinib resistance in RCC<sup>68</sup> and immune evasion in pancreatic cancer<sup>69</sup>; preliminary attempts to combine targeted or immune checkpoint inhibitors with lysosome inhibitors in the treatment of RCC might lead to new directions in the control of advanced tumors<sup>70,71</sup>, especially those with lung metastasis.

In summary, our work herein revealed the critical role of LAPT5, a lysosome transmembrane protein, in lung-specific metastasis. LAPT5 recruits WWP2 and mediates the ubiquitination, lysosomal sorting, and degradation of the critical BMP receptor BMP1A, thereby interfering with lung stroma-derived anti-metastatic BMP signals and ultimately promotes lung-specific metastasis. Our results suggested that LAPT5 may be a potential therapeutic target for lung metastasis of multiple cancer types.

## Methods

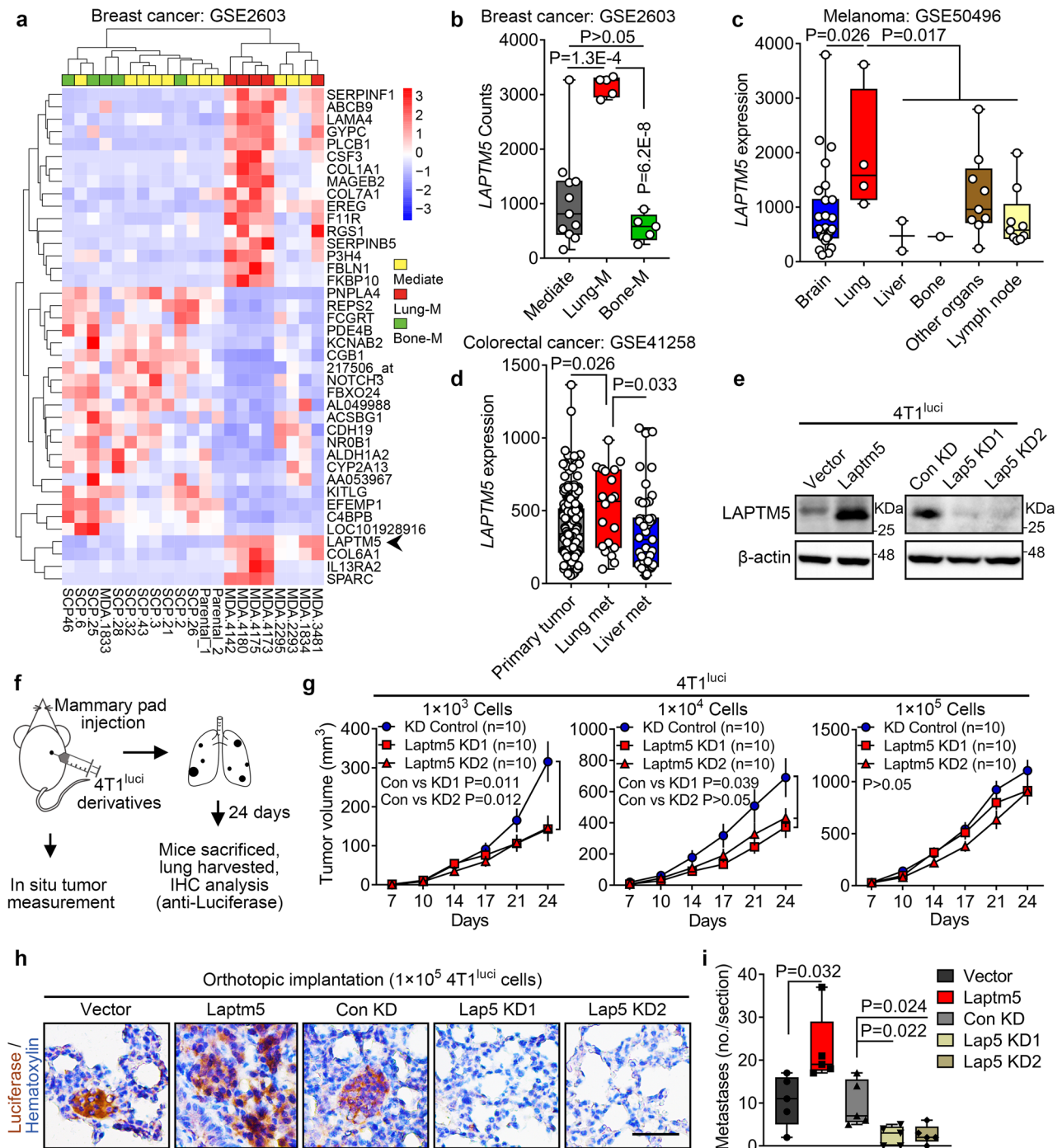
**Cell culture.** 786-O, 293T, 4T1, and MDA-MB-231 cells were obtained from the Cell Bank of the Chinese Academy of Science (Shanghai, China). Renca cells were purchased from ATCC. Cell line identity was confirmed by fingerprinting (Bio-Research Innovation Center, Suzhou, China). Renca and 4T1 cells were transfected with a lentivirus expressing firefly luciferase, 786-O cells were transfected with a lentivirus expressing enhanced GFP (eGFP) and firefly luciferase. Puromycin was added to sort luciferase and eGFP positive cells. 786-O, Renca, and 4T1 cells were cultured in RPMI 1640 medium with 10% fetal bovine serum (FBS). 293T and MDA-MB-231 cells were maintained in DMEM medium with 10% FBS. All complete mediums were supplemented with 100 U/mL penicillin and 100  $\mu$ g/mL streptomycin. Cultures were maintained at 37 °C under a humidified atmosphere containing 5% CO<sub>2</sub>.

**Plasmid, lentivirus construction, and transfection.** Small interfering RNAs (siRNAs) against human LAPT5 and WWP2 were purchased from GenePharma (Shanghai, China). Validated sequences were cloned into the vector pLKO.1-Puro to construct short hairpin RNAs (shRNAs). Flag-tagged human LAPT5 and His-tagged catalytically inactive mutant of WWP2 (cysteine in the 838th amino acid was replaced with alanine, WWP2<sup>C838A</sup>) vectors were purchased from OBiO Technology (Shanghai, China). HA-tagged ubiquitin was obtained from Addgene. Murine *Laptm5* and *Bmpr1a* coding sequences were cloned into the expression vector pCDH-CMV-Flag-EF1-Puro, while Myc-tagged human BMP1A, HA-tagged murine WWP2, HA-/His-tagged full-length and mutant truncated human WWP2 were cloned and expressed in a pcDNA3.1(-)-Puro vectors. Plasmids were transfected into cells using Lipofectamine 2000 per manufacturer’s instructions.

TET-inducible Flag-Laptm5/Control lentivirus were obtained from GeneChem (Shanghai, China). To produce lentivirus, 5  $\mu$ g pLP1, 2.5  $\mu$ g pLP2, 5  $\mu$ g pLP/VSVG plasmids, and 5  $\mu$ g vectors expressing control shRNA, specific shRNA constructs (against murine LAPT5), or human and murine LAPT5 were transfected into 293T cells with 70–80% confluence in 100 mm plate using Lipofectamine 2000. After incubation for 48–72 h, the supernatants containing lentivirus were harvested and used to infect target cells with polybrene for 12 h in the incubator. After selection with puromycin for 7 days, cells were harvested to determine the knockdown or overexpression efficiency.

**Mouse studies and isolation of lung-derived cells.** All animal studies were conducted according to the guidelines of the Institutional Animal Care and Use Committee of Nanjing Drum Tower Hospital.





For *in vivo* selection, a cell suspension containing  $1 \times 10^4$  Renca<sup>luc1</sup> in a volume of 100  $\mu$ L phosphate buffer solution (PBS) was injected into the left ventricle (LV) of anesthetized 6 to 8-week-old male BALB/c mice. Similarly, a cell suspension of  $1 \times 10^6$  786O<sup>luc1/eGFP</sup> was injected in the LV of 8-week-old male NOD/SCID mice. Mice were terminally anesthetized and intraperitoneal injected with D-Luciferin (150 mg per kg body weight, 10 min prior to imaging) to monitor metastasis by *in vivo* imaging with the IVIS Spectrum Imaging System (Caliper Life Sciences, MA, USA). Only organs revealing signal of metastasis were harvested and further confirmed by *ex vivo* imaging. After that, tumor nodules from organs were aseptically dissected and digested in 0.25% EDTA containing trypsin, and inoculated in complete RPMI 1640 medium to acquire tumor cells from representative organs. After reaching confluency, derivative cells were purified and re-injected into mice for the next round of isolation.

To validate metastatic organotropism of derivative cells, cells (Renca<sup>luc1</sup> and derivatives,  $1 \times 10^4$  cells; 786O<sup>luc1/eGFP</sup> and derivatives,  $1 \times 10^6$  cells) were injected intracardially. To examine the effect of LAPTM5 on organ metastasis, cells (control and Laptm5-overexpressing Renca<sup>luc1</sup>,  $1 \times 10^4$  cells; control and Laptm5-silenced Renca<sup>LuM2b</sup>,  $1 \times 10^4$  cells; and control and LAPTM5-overexpressing 786O<sup>luc1/eGFP</sup>,  $1 \times 10^6$  cells) were injected intracardially. Luminescence was monitored every 5–6 days. The change in photon flux was determined using quantitative region-of-interest (ROI) analysis. Bone metastases were further examined with the X-Ray model of IVIS Spectrum Imaging System.

To examine lung colonization, cells (control and Laptm5-overexpressing Renca<sup>luc1</sup>,  $1 \times 10^5$  cells; control and Laptm5-silenced Renca<sup>LuM2b</sup>,  $1 \times 10^5$  cells) were injected intravenously. Lungs were harvested at 1, 2, 7, 14, and 21 days after the injection. For the TET-inducible assays, Flag-Laptm5 (Tet-on) Renca<sup>luc1</sup> cells ( $1 \times 10^5$ ) were injected intravenously. Mice were administered with 2 mg/mL Dox in drinking water. Lungs were also harvested at 1, 2, 7, 14, and 21 days after injection. Lung metastatic lesions were confirmed by histological analysis.

For tumor initiation experiments, the indicated numbers ( $1 \times 10^3$ ,  $1 \times 10^4$ ,  $1 \times 10^5$ ) of cells were suspended in a 1:1 mixture of PBS and growth-factor-reduced Matrigel, and subcutaneously implanted in buttocks or orthotopically implanted in the subcapsular of mice (Renca<sup>luc1</sup> cells and derivatives), or injected into the mammary gland of 6 to 8-week-old female BALB/c mice (4T1<sup>luc1</sup> cells and derivatives). Primary tumor growth was monitored twice a week by taking measurements of tumor length (L) and width (W). Tumor volume was calculated using the formula  $LW^2/2$ . For orthotopic settings, tumor formation and growth were assessed 21 days after implantation by *in vivo* imaging.

**RNA isolation, semi-qPCR, and real-time qPCR.** Total RNA was extracted with TRIzol reagent. cDNA synthesis of genes involved using PrimeScript RT Master Mix. Semi-PCR and real-time qPCR involved use of ChamQ Universal SYBR qPCR Master Mix with the StepOne Real-Time PCR System (Thermo Fisher Scientific, MA, USA). Experiments were carried out according to the manufacturer's instructions. Data were acquired with QuantStudio 6 Flex Software v 1.3. Products of semi-PCR were separated by agarose gel electrophoresis. The fold change in the gene expression was calculated using the comparative *Ct* method, and two or three replicates were tested for each cDNA sample. *ACTB* or *Acb* were used as an internal reference. The sequences of the primers are listed in Supplementary Data 6.

**Library construction for RNA sequencing and sequencing procedures.** RNA was extracted from Renca<sup>Parental</sup>, Renca<sup>LuM2b</sup>, Renca<sup>BrM2b</sup>, and Renca<sup>BoM2</sup> during the logarithmic growth phase. A total amount of 3  $\mu$ g RNA per sample was used as input material for the RNA sample preparations. Sequencing libraries were generated using NEBNext® Ultra™ RNA Library Prep Kit for Illumina® (NEB, MA, USA) according to the manufacturer's instructions and index codes were added to attribute sequences to each sample. In order to select cDNA fragments of preferentially 250–300 bp in length, the library fragments were purified with AMPure XP system (Beckman Coulter, Beverly, USA). Then, 3  $\mu$ L USER Enzyme (NEB) was used with size-selected, adaptor-ligated cDNA at 37 °C for 15 min followed by 5 min at 95 °C before PCR. Then PCR was performed with Phusion High-Fidelity DNA polymerase, Universal PCR primers and Index (X) Primer. At last, PCR products were purified (AMPure XP system) and the quality of library was assessed on the Agilent Bioanalyzer 2100 system. Then, the index-coded samples were clustered on a cBot Cluster Generation System using TruSeq PE Cluster Kit v3-cBot-HS (Illumina, CA, USA) according to the manufacturer's instructions. After cluster generation, the library preparations were sequenced on an Illumina Novaseq platform and 125–150 bp paired-end reads were generated (NovoGene, Beijing, China).

**Immunoblotting (IB) and immunoprecipitation (IP).** Total cell extracts were prepared using RIPA buffer containing a cocktail of proteinase inhibitors and a cocktail of phosphatase inhibitors. Then, proteins were denatured at 95 °C for 5 min and then separated by SDS-PAGE, then transferred to 0.22  $\mu$ m PVDF membranes (Bio-Rad, Hercules, CA). After blocking with 5% skim milk, the membranes were incubated with specific primary antibodies overnight at 4 °C and secondary antibodies at room temperature (RT) for 1 h. Proteins were quantified using an electrochemiluminescence (ECL) system (Tanon, Shanghai, China). Data

were acquired using CLiNX platform and quantified using ImageJ 1.53 software. Polyclonal rabbit antibodies were raised against a peptide (PPKTPEGDPAPPY-SEV) located near the C terminus of mouse LAPTM5<sup>36</sup>.

For IP, after transfection or stimulation, cells were lysed in IP lysis buffer containing proteinase and phosphatase inhibitors. Specific primary antibodies were added to the lysates and incubated overnight at 4 °C, with homologous immunoglobulin G (IgG) as the control antibody. Then, Protein G Magnetic Beads (CST, MA, USA) were added in the system and incubated for 30 min at RT and then separated using the magnetic separation rack. Ultimately, conjoint proteins were eluted and sent for IB. Information on antibodies is provided in Supplementary Data 7.

**Immunofluorescence.** Briefly, cells were seeded on slides 24 h in advance. Then, culture medium was removed, and the cells were fixed with 4% paraformaldehyde (PFA) for 30 min. Cells were washed three times with PBS and permeabilized with 0.3% Triton X-100 for 15 min. Then cells were blocked with 5% BSA solution and incubated with specific primary antibodies overnight at 4 °C and fluorescence labelled secondary antibodies at RT for 1 h. Nuclei were stained with 0.2 mg/L DAPI for 5 min. Slides were observed and photographed using EVOS Auto 2 (Invitrogen) and EVOS FL Auto 2.0 Imaging System.

**TMT-labeled liquid chromatography-tandem mass spectrometry (LC-MS/MS).** 786-O<sup>LAPTM5</sup> and Renca<sup>Laptm5</sup> cells treated or untreated with 10 ng/mL BMP4 for 60 min were used for IP assays with anti-Flag and rabbit IgG as control. After SDS-PAGE and Coomassie brilliant blue staining, DTT was added to the IP products until the final concentration was 100 mM. The IP products were then boiled for 5 min and cooled to RT. Next, 200  $\mu$ L UA buffer was added and the products were then transferred to a 30 kD ultrafiltration tube, and centrifuged at 12,500  $\times$  g for 15 min. The filtrate was discarded and the remnant was re-centrifuged. Then, 100  $\mu$ L IAA buffer was added to the system (100 mM IAA in UA) and vortexed at 600 rpm for 1 min. The products were incubated in the dark at RT for 30 min, and centrifuged at 12,500  $\times$  g for 15 min. After that, 100  $\mu$ L UA buffer was added, followed by centrifugation at 12,500  $\times$  g for 15 min; and repeated again. Next, 100  $\mu$ L 0.1 M TEAB solution was added and centrifuged at 12,500  $\times$  g for 15 min, repeated twice. Next, 40  $\mu$ L Trypsin buffer (4  $\mu$ g trypsin in 40  $\mu$ L 0.1 M TEAB solution) was added and vortexed at 600 rpm for 1 min, then placed at 37 °C for 16–18 h. The products were transferred to a new collection tube and centrifuged at 12,500  $\times$  g for 15 min. Then 20  $\mu$ L 0.1 M TEAB solution was added and centrifuged at 12,500  $\times$  g for 15 min, and the filtrate was collected. Later, C18 Cartridge was used to desalt and lyophilize the peptides, then 10  $\mu$ L 0.1% formic acid was added to the peptides, and sent for TMT-labeled LC-MS/MS analysis (GeneChem, Shanghai, China). Data were collected with Thermo Q Exactive and software Proteome Discoverer 2.1.

**MTT assay.** Cultured cells in logarithmic phase were digested to obtain a cell suspension and seeded in 96-well plates (Renca and derivatives,  $2 \times 10^3$  cells/well; 786-O and derivatives,  $1 \times 10^4$  cells/well) and cultured in complete medium. After 12, 24, 48, 72 and 96 h, cells were incubated in 0.5 mg/mL MTT (3-(4,5-dimethylthiazol-2-yl)-2,5-diphenyl tetrazolium bromide) for 2 h at 37 °C. MTT crystals were dissolved in DMSO and absorbance was measured at a wavelength of 570 nm using Tecan i-control system.

**Transwell invasion assay.** Diluted matrigel (BD Biosciences) was spread on the bottom of the upper transwell chamber (8  $\mu$ m, Corning, NY, USA) and placed in 37 °C for 4 h to ensure matrigel condensation. The digested cells (Renca and derivatives,  $1 \times 10^5$  cells/well; 786-O and derivatives,  $2 \times 10^4$  cells/well) were seeded in the upper chamber to migrate, and incubated at 37 °C. After 24 h (Renca) or 10 h (786-O) incubation, chambers were fixed, then stained with the Crystal Violet Staining Solution (Beyotime), and counted under a light microscope.

**3D tumor sphere assay.** Single-cell suspensions (Renca,  $4 \times 10^4$  cells/mL; 786-O,  $1 \times 10^5$  cells/mL; 4T1,  $4 \times 10^4$  cells/mL; MDA-MB-231,  $1 \times 10^5$  cells/mL) were plated on ultra-low attachment plates (Corning) and cultured in serum-free RPMI 1640 or DMEM medium supplemented with 10 ng/mL epidermal growth factor (EGF) (Peprotech), 10 ng/mL fibroblast growth factor (FGF) (Peprotech) and 1 ng/mL B-27 (Peprotech) for 7 days. Tumor spheres were visualized by phase contrast microscope and photographed for counting.

**Clinical specimens.** Formalin-fixed RCC metastases from various organs (10 lung metastases, 22 bone metastases, 2 brain metastases), primary RCC tissues ( $n = 150$ ), and noncancerous kidney tissues ( $n = 106$ ) were collected from patients undergoing biopsies or surgical resection from 2005 to 2019. Cancerous tissue was classified according to the WHO classification. Patients' clinical and pathological information were collected and written informed consent was obtained from each patient. Ethics approval was obtained from the Nanjing University Medical School affiliated Nanjing Drum Tower Hospital.

**Hematein-eosin (H&E) and immunohistochemical (IHC) staining.** Paraformaldehyde fixed tissues were cut into 3  $\mu\text{m}$  slices and attached to a highly adherent slide. Next, slides were placed at 75 °C for 2 h, then dewaxed in xylene for 3 min thrice, and placed in 100, 90, 80, and 70% ethanol solution 2 min each to re-hydrate. For H&E staining, re-hydrated slides were stained in hematoxylin for 1 min and eosin for 1 min. For IHC staining, re-hydrated slides were blocked with 5% BSA solution and then incubated with specific primary antibodies overnight at 4 °C and HRP-linked secondary antibodies (OriGene, Beijing, China) at RT for 1 h. Finally, the detection was performed with DAB detection kit (ZsBio, Beijing, China). Data were acquired using Leica Microsystems and Leica Application Suite v 4.12.0. Multiple random fields on the slide were chosen for analyzing, staining intensity was scored as 0 (negative), 1 (low), 2 (moderate), 3 (high), and 4 (extremely high). Staining range was scored as percentage of each staining intensity. The final score was defined as the sum of product of the intensity scores and staining range; a score  $\leq 160$  was defined as low expression and  $> 160$  high expression in clinical samples.

**Bioinformatics analysis.** Array data for Jon\_Renal\_Cancer were obtained from the supplementary data of Jones' study (PMID: 16115910), while processed matrix array data for GSE2603, GSE50496, and GSE41258 were collected from Gene Expression Omnibus (GEO) database. GSEA was analyzed by pre-Ranked GSEA (preRankedGSEA) on genes ranked by Spearman correlation coefficient. Briefly, the spearman correlation coefficients between LAPTM5 and all other genes were calculated using TCGA KIRC or KIRP dataset, separately. The correlation coefficients were sorted in descending order and submitted to "GSEA" function of R "clusterProfiler" package with default parameters. The gene sets were obtained from the Molecular Signatures Database (MSigDB 7.1) and the pathways curated from the Pathway Interaction Database (PID) were used in this analysis. The GSEA results were further visualized by R "enrichplot" package.

**Statistical analysis.** The data presentation and statistical analyses are described in the figure legends.  $\chi^2$  test and univariate and multivariate analyses were performed with IBM SPSS Statistics 21 software. The remaining data analyses were performed by Graphpad Prism 7 software. Differences with P values  $< 0.05$  were considered statistically significant.

**Reporting summary.** Further information on research design is available in the Nature Research Reporting Summary linked to this article.

## Data availability

The RNA-seq data generated in this study have been deposited in the National Center for Biotechnology Information Sequence Read Archive (SRA) database under accession code PRJNA724865. Processed data of breast cancer (accession number: GSE2603), melanoma (accession number: GSE50496), and colorectal cancer (accession number: GSE41258); were collected from Gene Expression Omnibus (GEO) database. Processed data of Jon\_Renal\_Cancer were collected from supplementary information of this paper (<https://doi.org/10.1158/1078-0432.CCR-04-2225>)<sup>30</sup>. All the other data supporting the findings of this study are available within the article and its Supplementary Information files. A reporting summary for this article is available as a Supplementary Information file. Source data are provided with this paper.

Received: 17 July 2021; Accepted: 30 June 2022;

Published online: 16 July 2022

## References

- Mehlen, P. & Puisieux, A. Metastasis: A question of life or death. *Nat. Rev. Cancer* **6**, 449–458 (2006).
- Bianchi, M. et al. Distribution of metastatic sites in renal cell carcinoma: A population-based analysis. *Ann. Oncol.* **23**, 973–980 (2012).
- Kennecke, H. et al. Metastatic behavior of breast cancer subtypes. *J. Clin. Oncol.* **28**, 3271–3277 (2010).
- Botticelli, A. et al. The agnostic role of site of metastasis in predicting outcomes in cancer patients treated with immunotherapy. *Vaccines* <https://doi.org/10.3390/vaccines8020203> (2020).
- Ozawa, H. et al. A single-centre, retrospective, observational analysis of fulvestrant for recurrent/metastatic breast cancer according to metastatic site. *Anticancer Res.* **39**, 5653–5662 (2019).
- Klein, C. A. Cancer progression and the invisible phase of metastatic colonization. *Nat. Rev. Cancer* **20**, 681–694 (2020).
- Nguyen, D. X., Bos, P. D. & Massagué, J. Metastasis: From dissemination to organ-specific colonization. *Nat. Rev. Cancer* **9**, 274–284 (2009).
- Valastyan, S. & Weinberg, R. A. Tumor metastasis: Molecular insights and evolving paradigms. *Cell* **147**, 275–292 (2011).
- Valiente, M. et al. Serpins promote cancer cell survival and vascular co-option in brain metastasis. *Cell* **156**, 1002–1016 (2014).
- Giaume, C., Koulakoff, A., Roux, L., Holcman, D. & Rouach, N. Astroglial networks: A step further in neuroglial and gliovascular interactions. *Nat. Rev. Neurosci.* **11**, 87–99 (2010).
- Ren, D. et al. Wnt5a induces and maintains prostate cancer cells dormancy in bone. *J. Exp. Med.* **216**, 428–449 (2019).
- Yu-Lee, L. Y. et al. Osteoblast-secreted factors mediate dormancy of metastatic prostate cancer in the bone via activation of the TGF $\beta$ RIII-p38MAPK-pS249/T252RB pathway. *Cancer Res.* **78**, 2911–2924 (2018).
- Gao, H. et al. The BMP inhibitor Coco reactivates breast cancer cells at lung metastatic sites. *Cell* **150**, 764–779 (2012).
- Schild, T., Low, V., Blenis, J. & Gomes, A. P. Unique metabolic adaptations dictate distal organ-specific metastatic colonization. *Cancer Cell* **33**, 347–354 (2018).
- Chen, Q. et al. Carcinoma-astrocyte gap junctions promote brain metastasis by cGAMP transfer. *Nature* **533**, 493–498 (2016).
- Croset, M. et al. miRNA-30 family members inhibit breast cancer invasion, osteomimicry, and bone destruction by directly targeting multiple bone metastasis-associated genes. *Cancer Res.* **78**, 5259–5273 (2018).
- Campbell, P. J. et al. The patterns and dynamics of genomic instability in metastatic pancreatic cancer. *Nature* **467**, 1109–1113 (2010).
- Huang, R. & Rofstad, E. K. Integrins as therapeutic targets in the organ-specific metastasis of human malignant melanoma. *J. Exp. Clin. Cancer Res.* **37**, 92 (2018).
- Minn, A. J. et al. Genes that mediate breast cancer metastasis to lung. *Nature* **436**, 518–524 (2005).
- Bos, P. D. et al. Genes that mediate breast cancer metastasis to the brain. *Nature* **459**, 1005–1009 (2009).
- Kang, Y. et al. A multigenic program mediating breast cancer metastasis to bone. *Cancer Cell* **3**, 537–549 (2003).
- Bissig, H., Richter, J. & Desper, R. Evaluation of the clonal relationship between primary and metastatic renal cell carcinoma by comparative genomic hybridization. *Am. J. Pathol.* **155**, 267–274 (1999).
- Junker, K. et al. Genetic profile of bone metastases in renal cell carcinoma. *Eur. Urol.* **45**, 320–324 (2004).
- Birkbak, N. J. & McGranahan, N. Cancer genome evolutionary trajectories in metastasis. *Cancer Cell* **37**, 8–19 (2020).
- Reiter, J. G. et al. Minimal functional driver gene heterogeneity among untreated metastases. *Science* **361**, 1033–1037 (2018).
- Turajlic, S. et al. Tracking cancer evolution reveals constrained routes to metastases: TRACERx renal. *Cell* **173**, 581–594 e512 (2018).
- Flanigan, R. C. et al. Nephrectomy followed by interferon alfa-2b compared with interferon alfa-2b alone for metastatic renal-cell cancer. *N. Engl. J. Med.* **345**, 1655–1659 (2001).
- McKay, R. R. et al. Impact of bone and liver metastases on patients with renal cell carcinoma treated with targeted therapy. *Eur. Urol.* **65**, 577–584 (2014).
- Motzer, R. J. et al. Prognostic factors for survival in 1059 patients treated with sunitinib for metastatic renal cell carcinoma. *Br. J. Cancer* **108**, 2470–2477 (2013).
- Jones, J. et al. Gene signatures of progression and metastasis in renal cell cancer. *Clin. Cancer Res.* **11**, 5730–5739 (2005).
- Adra, C. N., Zhu, S., Ko, J. L. & Guillemot, J. C. LAPTM5: A novel lysosomal-associated multispansing membrane protein preferentially expressed in hematopoietic cells. *Genomics* **35**, 328–337 (1996).
- Celia-Terrassa, T. & Kang, Y. B. Distinctive properties of metastasis-initiating cells. *Genes Dev.* **30**, 892–908 (2016).
- Altorki, N. K. et al. The lung microenvironment: An important regulator of tumour growth and metastasis. *Nat. Rev. Cancer* **19**, 9–31 (2019).
- Hu, J. et al. Endoglin is essential for the maintenance of self-renewal and chemoresistance in renal cancer stem cells. *Stem Cell Rep.* **9**, 464–477 (2017).
- Ouchida, R., Kurosaki, T. & Wang, J. Y. A role for lysosomal-associated protein transmembrane 5 in the negative regulation of surface B cell receptor levels and B cell activation. *J. Immunol.* **185**, 294–301 (2010).
- Ouchida, R. et al. A lysosomal protein negatively regulates surface T cell antigen receptor expression by promoting CD3zeta-chain degradation. *Immunity* **29**, 33–43 (2008).
- Kawai, Y. et al. LAPTM5 promotes lysosomal degradation of intracellular CD3 $\zeta$  but not of cell surface CD3 $\zeta$ . *Immunol. Cell Biol.* **92**, 527–534 (2014).
- Song, K. H. et al. GALNT14 promotes lung-specific breast cancer metastasis by modulating self-renewal and interaction with the lung microenvironment. *Nat. Commun.* **7**, 13796 (2016).
- Katagiri, T. & Watabe, T. Bone morphogenetic proteins. *Cold Spring Harbor Perspect. Biol.* <https://doi.org/10.1101/cshperspect.a021899> (2016).
- Murakami, K. & Etlinger, J. D. Role of SMURF1 ubiquitin ligase in BMP receptor trafficking and signaling. *Cell Signal* **54**, 139–149 (2019).
- Harvey, K. F., Dinudom, A., Cook, D. I. & Kumar, S. The Nedd4-like protein KIAA0439 is a potential regulator of the epithelial sodium channel. *J. Biol. Chem.* **276**, 8597–8601 (2001).



42. Rotin, D. & Kumar, S. Physiological functions of the HECT family of ubiquitin ligases. *Nat. Rev. Mol. Cell Biol.* **10**, 398–409 (2009).
43. Vergarajauregui, S., Martina, J. A. & Puertollano, R. LAPTMs regulate lysosomal function and interact with mucopolipin 1: New clues for understanding mucopolipidosis type IV. *J. Cell Sci.* **124**, 459–468 (2011).
44. Pak, Y., Glowacka, W. K., Bruce, M. C., Pham, N. & Rotin, D. Transport of LAPTMs to lysosomes requires association with the ubiquitin ligase Nedd4, but not LAPTMs ubiquitination. *J. Cell Biol.* **175**, 631–645 (2006).
45. Burr, M. L. et al. CMTM6 maintains the expression of PD-L1 and regulates anti-tumour immunity. *Nature* **549**, 101–105 (2017).
46. Yang, Y. et al. E3 ligase WWP2 negatively regulates TLR3-mediated innate immune response by targeting TRIF for ubiquitination and degradation. *Proc. Natl Acad. Sci. USA* **110**, 5115–5120 (2013).
47. Chen, G. et al. Molecular profiling of patient-matched brain and extracranial melanoma metastases implicates the PI3K pathway as a therapeutic target. *Clin. Cancer Res.* **20**, 5537–5546 (2014).
48. Sheffer, M. et al. Association of survival and disease progression with chromosomal instability: A genomic exploration of colorectal cancer. *Proc. Natl Acad. Sci. USA* **106**, 7131–7136 (2009).
49. Yin, X. et al. Assessment for prognostic value of differentially expressed genes in immune microenvironment of clear cell renal cell carcinoma. *Am. J. Transl. Res.* **12**, 5416–5432 (2020).
50. Zabkiewicz, C., Resaul, J., Hargest, R., Jiang, W. G. & Ye, L. Bone morphogenetic proteins, breast cancer, and bone metastases: Striking the right balance. *Endocr. Relat. Cancer* **24**, R349–r366 (2017).
51. Chen, D., Zhao, M. & Mundy, G. R. Bone morphogenetic proteins. *Growth Factors* **22**, 233–241 (2004).
52. Zou, M. L. et al. The smad dependent TGF- $\beta$  and BMP signaling pathway in bone remodeling and therapies. *Front. Mol. Biosci.* **8**, 593310 (2021).
53. Lambert, A. W., Pattabiraman, D. R. & Weinberg, R. A. Emerging biological principles of metastasis. *Cell* **168**, 670–691 (2017).
54. Colland, F. et al. Functional proteomics mapping of a human signaling pathway. *Genome Res.* **14**, 1324–1332 (2004).
55. Dabestani, S. et al. Renal cell carcinoma recurrences and metastases in primary non-metastatic patients: A population-based study. *World J. Urol.* **34**, 1081–1086 (2016).
56. Noguchi, G. et al. Time-dependent change in relapse sites of renal cell carcinoma after curative surgery. *Clin. Exp. Metastasis* **35**, 69–75 (2018).
57. Bryant, K. L. et al. Combination of ERK and autophagy inhibition as a treatment approach for pancreatic cancer. *Nat. Med.* **25**, 628–640 (2019).
58. Carew, J. S. et al. Disruption of autophagic degradation with ROC-325 antagonizes renal cell carcinoma pathogenesis. *Clin. Cancer Res.* **23**, 2869–2879 (2017).
59. Cook, K. L. et al. Hydroxychloroquine inhibits autophagy to potentiate antiestrogen responsiveness in ER+ breast cancer. *Clin. Cancer Res.* **20**, 3222–3232 (2014).
60. Maes, H. et al. Tumor vessel normalization by chloroquine independent of autophagy. *Cancer Cell* **26**, 190–206 (2014).
61. Kinsey, C. G. et al. Protective autophagy elicited by RAF→MEK→ERK inhibition suggests a treatment strategy for RAS-driven cancers. *Nat. Med.* **25**, 620–627 (2019).
62. McAfee, Q. et al. Autophagy inhibitor Lys05 has single-agent antitumor activity and reproduces the phenotype of a genetic autophagy deficiency. *Proc. Natl Acad. Sci. USA* **109**, 8253–8258 (2012).
63. Wolpin, B. M. et al. Phase II and pharmacodynamic study of autophagy inhibition using hydroxychloroquine in patients with metastatic pancreatic adenocarcinoma. *Oncologist* **19**, 637–638 (2014).
64. Karasic, T. B. et al. Effect of gemcitabine and nab-paclitaxel with or without hydroxychloroquine on patients with advanced pancreatic cancer: A phase 2 randomized clinical trial. *JAMA Oncol.* **5**, 993–998 (2019).
65. Rosenfeld, M. R. et al. A phase I/II trial of hydroxychloroquine in conjunction with radiation therapy and concurrent and adjuvant temozolomide in patients with newly diagnosed glioblastoma multiforme. *Autophagy* **10**, 1359–1368 (2014).
66. Patel, S. et al. Vorinostat and hydroxychloroquine improve immunity and inhibit autophagy in metastatic colorectal cancer. *Oncotarget* **7**, 59087–59097 (2016).
67. Arnaout, A. et al. A randomized, double-blind, window of opportunity trial evaluating the effects of chloroquine in breast cancer patients. *Breast Cancer Res. Treat.* **178**, 327–335 (2019).
68. Giuliano, S. et al. Resistance to sunitinib in renal clear cell carcinoma results from sequestration in lysosomes and inhibition of the autophagic flux. *Autophagy* **11**, 1891–1904 (2015).
69. Yamamoto, K. et al. Autophagy promotes immune evasion of pancreatic cancer by degrading MHC-I. *Nature* **581**, 100–105 (2020).
70. Li, M. L. et al. Chloroquine potentiates the anticancer effect of sunitinib on renal cell carcinoma by inhibiting autophagy and inducing apoptosis. *Oncol. Lett.* **15**, 2839–2846 (2018).
71. Haas, N. B. et al. Autophagy inhibition to augment mTOR inhibition: A phase I/II trial of everolimus and hydroxychloroquine in patients with previously treated renal cell carcinoma. *Clin. Cancer Res.* **25**, 2080–2087 (2019).

## Acknowledgements

This work was supported by grants from the National Natural Science Foundation of China (82002681, 81772710, 81972388, 82070703, 81972387 and 21877060), the Natural Science Foundation of Jiangsu Province (BK20200123) and the Project of Invigorating Health Care through Science, Technology and Education Jiangsu Provincial Key Medical Discipline (ZDXKB2016014). We thank Vazyme Biotech for the production of polyclonal antibodies against mouse LAPTMs.

## Author contributions

H.G., B.J., and X.Z. devised and coordinated the project. B.J. performed all the experiments with help from W.C. (the third author), W.D., M.D., W.M.C., H.Q., W.C. (the ninth author), J.G., M.C., K.H., T.L., and Y.D. B.L. performed bioinformatics analyses. B.J., W.D., and K.H. performed experiments with the Renca metastasis model. Y.F. collected clinical samples and performed IHC analysis. B.J., C.Y., and H.G. wrote the manuscript. All authors revised the manuscript.

## Competing interests

The authors declare no competing interests.

## Additional information

**Supplementary information** The online version contains supplementary material available at <https://doi.org/10.1038/s41467-022-31783-6>.

**Correspondence** and requests for materials should be addressed to Chao Yan or Hongqian Guo.

**Peer review information** *Nature Communications* thanks Leigh Fremuth and the other, anonymous, reviewer(s) for their contribution to the peer review of this work. Peer reviewer reports are available.

**Reprints and permission information** is available at <http://www.nature.com/reprints>

**Publisher's note** Springer Nature remains neutral with regard to jurisdictional claims in published maps and institutional affiliations.



**Open Access** This article is licensed under a Creative Commons Attribution 4.0 International License, which permits use, sharing, adaptation, distribution and reproduction in any medium or format, as long as you give appropriate credit to the original author(s) and the source, provide a link to the Creative Commons license, and indicate if changes were made. The images or other third party material in this article are included in the article's Creative Commons license, unless indicated otherwise in a credit line to the material. If material is not included in the article's Creative Commons license and your intended use is not permitted by statutory regulation or exceeds the permitted use, you will need to obtain permission directly from the copyright holder. To view a copy of this license, visit <http://creativecommons.org/licenses/by/4.0/>.

© The Author(s) 2022